



Kinetic Monte Carlo simulations of Ge–Sb–Te thin film crystallization

A Portavoce, G Roland, J Remondina, M Descoins, M Bertoglio, M Amalraj,
P Eyméoud, D Dutartre, F Lorut, M Putero

► To cite this version:

A Portavoce, G Roland, J Remondina, M Descoins, M Bertoglio, et al.. Kinetic Monte Carlo simulations of Ge–Sb–Te thin film crystallization. *Nanotechnology*, 2022, 33 (29), pp.295601. 10.1088/1361-6528/ac6813 . hal-04008115

HAL Id: hal-04008115

<https://hal.science/hal-04008115>

Submitted on 28 Feb 2023

HAL is a multi-disciplinary open access archive for the deposit and dissemination of scientific research documents, whether they are published or not. The documents may come from teaching and research institutions in France or abroad, or from public or private research centers.

L'archive ouverte pluridisciplinaire **HAL**, est destinée au dépôt et à la diffusion de documents scientifiques de niveau recherche, publiés ou non, émanant des établissements d'enseignement et de recherche français ou étrangers, des laboratoires publics ou privés.

Kinetic Monte Carlo simulations of Ge–Sb– Te thin film crystallization

A. Portavoce^{1,*}, G. Roland^{1,2}, J. Remondina¹, M. Descoins¹, M. Bertoglio¹, M. Amalraj¹, P. Eymeoud¹, D. Dutartre², F. Lorut², M. Putero¹

¹*Aix-Marseille University/CNRS, IM2NP, Faculté des Sciences de Saint-Jérôme case 142, 13397 Marseille, France*

²*STMicroelectronics, 850 Rue Jean Monnet, 38920 Crolles, France*

ABSTRACT

Simulation of atomic redistribution in Ge-Sb-Te (GST)-based memory cells during SET/RESET cycling is needed in order to understand GST memory cell failure and to design improved non-volatile memories. However, this type of atomic scale simulations is extremely challenging since the simulation cell should consider about 200000 atoms, the three elements Ge, Sb, and Te are of different nature (semiconductor, metal, and semi-metal, respectively), possess different lattice structure (diamond, rhombohedral, and hexagonal, respectively), and the amorphous-crystalline as well as the solid-liquid transitions of several binary and ternary phases need to be simulated.

In this work, we propose to use a simplified GST system in order to catch the basics of atomic redistribution in Ge-rich GST (GrGST) films using atomistic kinetic Monte Carlo (KMC) simulations. First, the influence of Ge excess on GST225 and Ge crystallization in 200-nm thick GrGST films was investigated experimentally and compared to the KMC simulations during isothermal or ramp annealing. Then, the model was used to simulate atomic redistribution in GrGST films during SET/RESET cycling. The KMC model is based on first-neighbor interactions on a face-centered-cubic rigid lattice using the tight-binding Ising model and direct exchanges between first-neighbor sites. Order-disorder transitions are used to model amorphous-crystalline transitions at low temperature and solid-liquid transitions at high temperature.

Good agreements were observed between experiments and simulations regarding the influence of Ge excess on GST225 and Ge crystallization, as well as concerning the growth kinetic of GST in GrGST films. Diverse RESET conditions, as well as the use of amorphous layers exhibiting the GST phase stoichiometry (seed layer) located at the bottom or at the top of the GrGST layer, were investigated during SET/RESET cycling simulations. The simulations showed different behaviors for stoichiometric and non-stoichiometric GST phases. The film microstructure stabilized during cycling is different for the two types of GST phase. Furthermore, the film microstructure was found to be independent of the RESET conditions in the case of stoichiometric GST, while it was found to be significantly dependent of both RESET conditions and the use of seed layers in the case of non-stoichiometric GST.

Keywords: Phase change memory, Phase change material, GST, Thin films, crystallization, Kinetic Monte Carlo simulation

*Corresponding author: alain.portavoce@im2np.fr

1. Introduction

The development of new applications, such as linked to the Internet-of-Things technology, requires a new generation of non-volatile memory displaying higher speeds of Write (SET, logical state '1') and Erase (RESET, logical state '0') processes and high endurance for data processing, combined with high retention capability and good scalability for data storage, exhibiting also a high power efficiency and low production cost [1]. Meeting most of these requirements, phase-change random access memories (PCRAM) are expected to become the leading technology of non-volatile memories [1,2,3,4]. PCRAM are based on the significant resistivity contrast between the amorphous state (high resistivity) and the crystalline state (low resistivity) of a class of chalcogenide materials so-called phase-change materials (PCM) [2,3]. The electrical resistivity difference between amorphous and crystalline PCM thin films can exhibit 6 orders of magnitude [4,5,6]. PCRAM operate at low voltage and show much faster switching speed compared to common Flash devices, with a Write-time in the nanosecond order instead of $\sim 100 \mu\text{s}$ for usual Flash memories [4], as well as a higher data storage stability due to the physical nature of the bit, relying on a structural modification of the material and not on the storage of an electric charge in the material [2,3,4]. Furthermore, PCM compatibility with conventional CMOS platforms and the possibility of integrating PCM in the back-end of the production process are technologically very appealing [7,8]. However, depending on the application, long-term stability of PCM can be an issue and has to be improved by material design [1].

Among PCM, GST alloys or compounds based on germanium (Ge), antimony (Sb), and tellurium (Te) were shown to possess high speed reversibility between the amorphous and crystalline states, as well as the required properties for the production of low power consumption non-volatile memories with high data retention, high degree of scalability, and multilevel storage

capability [4,2,3]. Generally, the crystallization process (SET) is slower than amorphization (RESET) [2,3,4]. The GST needs to be heated at a temperature above its crystallization temperature for SET, involving solid-state atomic redistribution and corresponding to a time \sim 100-500 ns. RESET requires higher temperatures and shorter times (\sim 50-100 ns) in order to melt and subsequently quench the material in an amorphous state.

The amorphous-crystal transition temperature is strongly dependent on the heating rate, GST interfaces, and the composition of the GST alloy [1]. The compound $\text{Ge}_2\text{Sb}_2\text{Te}_5$ (GST225) is the GST the most studied, offering a good compromise between crystallization speed and amorphous stability, [1,4,9,10]. GST225 crystallization occurs at the temperature $T_x^{225} \sim 423$ -443 K. At that temperature, amorphous GST225 (a-GST225) transforms into a metastable face-centred-cubic (fcc) phase exhibiting the ‘Rock Salt’ structure (c-GST225) [1,4]. This metastable phase is expected to contain a great amount of vacancies (\sim 20%) depending on the material composition, suggesting stoichiometry variations [11,12]. At higher temperature (\sim 703-723 K) a second structural transition is observed from the fcc metastable phase to a stable phase exhibiting a hexagonal close-packed (hcp) structure [1,4]. This hcp phase melts at $T_m^{225} \sim 873$ K. With $T_x^{225} \sim 423$ K, the GST225 presents two main concerns impeding its industrial development [7,8]: a-GST225 cannot maintain the stored data after soldering, as it usually involves increasing the temperature up to \sim 523 K for two minutes, and it cannot match automotive standards requiring two years of data retention at 423 K. In order to solve these limitations, the use of Ge-rich GST is currently investigated, as the crystallization temperature of Ge-rich GST was shown to increase with Ge content, allowing for high data retention on higher temperature range [7,8]. For example, $T_x^{225} \sim 643$ K was demonstrated for Ge-rich GST thin films and memory cells [7].

Ge-rich GST alloys exhibiting a Ge concentration above 30% (GrGST) are very promising for industrial memory applications [7,8]. However, the GrGST crystallization being

more complex due to the Ge addition, detailed understanding of atomic redistribution during cycling is needed. In situ TEM observations performed in 100 nm-thick GrGST films [13, 14] showed that the crystallization follows several stages: i) Ge/GST225 phase separation is first initiated in the amorphous phase (a-GrGST), then ii) Ge randomly nucleates in the film, followed by iii) the formation of the fcc GST225 phase, and finally iv) these two phases grow concurrently until reaching a metastable microstructure. Large GST225 grains (~ 50-100 nm) are surrounded by the Ge phase made of small Ge grains (~ 10 nm) at the end of the crystallization. The stable hcp-GST225 phase was not observed despite annealing temperatures significantly above the fcc-GST225/hcp-GST225 transition temperature. This may be explained by the composition analyzes suggesting that the GST225 grains are different from the regular GST225 stoichiometry, the grains being enriched with Ge and Sb [14]. The increase of the crystallization temperature observed in GrGST was also suggested to result from the Ge enrichment of the GST225 phase, since the composition of the GST phase may significantly vary along the pseudo-binary GeTe-Sb₂Te₃ tie line [13]. GrGST thin film crystallization follows the classical scheme composed of random nucleation, growth, and grain coalescence, which is piloted and kinetically limited by atomic transport [13, 14, 15].

Usual crystallization experiments are performed on as-deposited thin films annealed at constant temperature, aiming to simulate the SET operation. However, the SET process could involve a temperature gradient, the highest temperature being located at the interface with the “Heater” [3, 4, 7]. Furthermore, the RESET is difficult to investigate experimentally on thin films. Consequently, experimental information concerning atomic redistribution involved in multiple cycling is scarce. However, atomic redistribution in GrGST during cycling is expected to play a crucial role in reliability control as well as in prediction of PCRAM devices. Variations of material composition resulting from cycling may be the source of device failures and can

compromise the memory endurance [3,8,16]. PCM resistivity variation influences the power efficiency and the stability of memory cells, and was shown to depend on several factors such as thickness, heating rate, fabrication methods and conditions [1,4]. For example, amorphous state instability after repeated cycling is one of the main issues of PCRAM [3,16]. Thus, the understanding of atomic scale processes is crucial for the optimization of memory performance. How multiple cycling modifies atomic distribution in the memory cell and how the atomic redistribution influences device properties is of major interest. For example, GST-based PCRAM failure induced by gradual segregation of Ge, Sb, Te elements in different regions of the device was reported [17,18], and resistance drift in SET and RESET states has been observed [8]. Furthermore, alloys with reduced Te concentrations exhibit a reduced programming window [4] and dopant grain boundary segregation can suppress grain growth, resulting in higher transition temperature [4].

Static and molecular dynamic Ab initio calculations have been intensively performed on GST materials aiming to understand GST structure and properties from the atomic scale [12,20,21,22]. Ab initio simulations allowed important insights into structural, electronic, and bonding properties of GST, as well as on the fast crystallization and relaxation of the amorphous phase to be obtained. For example, electron transport properties in the GST225 such as the conductance and current-voltage curves were simulated in the amorphous and crystalline states [22]. Ab initio results suggest that PCM are characterized by generic bonding mechanisms, and three bonding models have been proposed so far: the resonant-bonding model [29,30], the metavalent-bonding model [31,32], and the hyperbonding model [25,26]. Concerning GST225, the two classical crystallization stages, homogeneous nucleation and growth, were identified [23,24,27]. The critical nucleus size was estimated to be below 50 atoms, and the switching time and the growth rate were found to be ~ 0.5 ns [12,23] and between 1 and 5 m s⁻¹ [12,24], respectively. High

atomic mobility was shown to be a prerequisite for fast growth [12]. The concentration and the nature of charge carriers in PCM could be determined [33], and the vacancy concentration was shown to have a strong role on charge carrier concentration in GST [28,34]. The electron mean free path in GST225 was estimated to be ~ 10 nm [22].

All these results are of prime importance for the development of PCRAM technology. However, the ability of simulating atomic redistribution during the cycling of GrGST-based memory is still needed in order to understand device failure and ageing, as well as to design upgraded memories. Conventional devices use the “mushroom-type” geometry [4,8]: a crystalline GST line with a section of 50×50 nm² is used as base material. It is covered with electrodes on its top and bottom, and a 50 nm-wide conductive element (the “Heater”) is periodically plugged along the GST line. The Heater is used to locally heat the GST to form a local memory point in a shape of an amorphous (RESET) or crystalline (SET) dome. Thus, the memory cell exhibits a lateral size of about 50 nm and contains a GST dome with a lateral size ~ 30 nm located above a Heater. The simulation of the atomic distribution in such a 50×50 nm² memory cell requires the use of a simulation cell containing about 200000 atoms. This type of simulations cannot be performed using ab initio methods, current ab initio cells containing about 400 to 1000 atoms. Furthermore, the kinetic Monte Carlo (KMC) method performed on a rigid lattice [36] is the technique of choice for the simulation of atomic redistribution versus time. The Monte Carlo technique has been used to simulate charge transport in amorphous GST225 [37], as well as to model the resistance evolution of embedded PCM based on GrGST [38]. However, KMC simulations have not been reported so far concerning phase transition simulation in GrGST memory cells. Indeed, the simulation of atomic redistribution and especially the solid-liquid transition in a GST layer raises several technical difficulties: i) GST is a ternary system

composed of three binary phase diagrams made of several phases with different melting temperatures, ii) the three elements Ge, Sb, and Te are of different nature: semiconductor, metal and semi-metal, respectively, and exhibit different structures: cubic diamond, rhombohedral, and hexagonal, respectively, and iii) the three states amorphous, crystalline, and liquid should be simulated. No known semi-empirical potential can be used to model atomic interactions for such case, and the atomic relaxation needed to simulate the amorphous and the liquid states should lead to unworkable calculation times.

The simulation of atomic redistribution in a memory cell considering the exact Ge-Sb-Te ternary system being extremely challenging, the simulation of an approached ternary GST^{*} system is suggested in the present work, using simplified considerations. In order to take into account size and time scales compatible with experiments, atomistic KMC simulations are performed on a fcc rigid lattice; the solid-liquid transition is substituted by the order-disorder transition; atomic interactions are modeled by first-neighbor pairwise interactions, and atoms are moved using the direct exchange process between first-neighbor lattice sites [39,40]. This type of simulations cannot reproduce the different phase structure, the exact phase diagrams, complex atomic interactions, the real atomic mechanisms... However, the system can be parametrized with the experimental phases' energies (cohesive energies and melting temperatures, for example) and the experimental kinetic parameters of atomic processes (diffusion and segregation activation energies, for example). The KMC simulations give the exact solution of the evolution of a thermodynamic non-regular solid solution taking into account the thermodynamic equilibrium driving forces and the atomic transport and ordering kinetics, including surface and interface energies. These simulations allow calculations to be fast, as well as interpretations based on thermodynamic and kinetics considerations [39,40]. In our case, the ordered solutions are

considered to correspond to crystalline phases, while disordered solutions (i.e. random atomic distributions) correspond to the amorphous state below T_m or to the liquid state above T_m .

The first part of the study concerns experimental measurements investigating the influence of Ge excess on GrGST crystallization. In situ X-ray diffraction (XRD) during both ramp and isothermal annealing was used to follow the crystallization kinetics of 200 nm-thick GrGST films with four different Ge excess. The experimental results were used to evaluate the relevance of the simulations before to simulate SET/RESET cycling of the film. Good qualitative agreement was found between experiments and simulations regarding Ge excess effect on both GST and Ge crystallization in GrGST films. Furthermore, a good agreement was also found concerning GST crystallization kinetics considering the GST phase exhibiting a non-negligible off-stoichiometry as well as a disorder character. SET/RESET KMC simulations showed that the evolution of the film microstructure is different for stoichiometric and non-stoichiometric GST. Cycling leads to the formation of a Ge/GST multilayer structure oriented in the direction perpendicular to the film surface for stoichiometric GST, while it promotes the formation of GST domains surrounded by Ge for non-stoichiometric GST. The stabilized microstructure is independent of RESET conditions in the case of stoichiometric GST, but is strongly dependent of RESET conditions in the case of non-stoichiometric GST. The use of seed layers (amorphous layers with the GST stoichiometry) at the top or at the bottom of the GrGST film can allow the GST to be in contact with the two electrodes instead of Ge.

2. Experiments

Ge, Sb and Te were co-deposited at room temperature (RT) on a substrate made of a 20 nm-thick TiN layer deposited on a Si(001) substrate. A 99.9999% pure Ar gas flow was used to simultaneously sputter a 99.999% pure Ge target, a 99.99% pure Sb target, and a 99.99% pure Te

target in a commercial magnetron sputtering system exhibiting a base pressure of 10^{-8} Torr. The Ge and Sb targets were sputtered in the DC mode, while the Te target was sputtered in the RF mode. The substrate was rotating at the rate of 5 rpm during deposition in order to provide GrGST films with homogeneous thickness. The Ge, Sb and Te fluxes were separately calibrated, measuring the thicknesses of several films (single element) deposited in different conditions by X-ray reflectivity (XRR). Five GST films were deposited with the same thickness ~ 200 nm, but with different Ge excess (E_x): i) $E_x = 0$ (225 stoichiometry: 22 at% Ge, 22 at% Sb, and 56 at% Te), ii) $E_x \sim 23\%$ (40 at% Ge, 17 at% Sb, and 43 at% Te), iii) $E_x \sim 42\%$ (55 at% Ge, 13 at% Sb, and 32 at% Te), iv) $E_x \sim 49\%$ (60 at% Ge, 11 at% Sb, and 29 at% Te), and v) $E_x \sim 61\%$ (70 at% Ge, 9 at% Sb, and 21 at% Te).

After co-deposition, the samples were annealed at constant temperature (isotherm) or following a heating ramp *in situ* in an XRD setup under a vacuum of $\sim 5 \times 10^{-5}$ Torr. All the XRD measurements were performed in a PANalytical Empyrean diffractometer using Cu radiation ($\lambda_{K\alpha} = 0.154$ nm) and a rapid detector (PANalytical PIXcel) in Bragg–Brentano geometry. The heating ramp in the XRD setup was 2 K min^{-1} , while the XRD acquisition time was 1 minute-long. The XRD measurements were performed between RT and a maximum temperature of 630 K.

3. Atomistic kinetic Monte Carlo simulations

The KMC simulations were performed on a rigid fcc atomic lattice. Energetics was based on the tight binding Ising model (TBIM), which is an effective Ising Hamiltonian derived from electronic-structure calculations ^[41]. The energetic model was initially developed for binary systems, made of two elements that are first noted A and B for example. The total energy of the

binary system is decomposed into pairwise interactions between first neighbors ε^{AA} , ε^{BB} , and ε^{AB} (with $\varepsilon \leq 0$). This description is not used to determine the absolute energy of the system, but to calculate the energy variations ΔU between configurations (atomic reordering) in the KMC scheme. The TBIM allows the difference in surface energies between the A and B elements $\Delta\gamma = Z_s(\varepsilon^{AA} - \varepsilon^{BB})$ as well as the essential thermodynamics of the A_cB_{1-c} alloy to be preserved through a single parameter $V^{AB} = 2\varepsilon^{AB} - \varepsilon^{AA} - \varepsilon^{BB}$ (Z_s is the number of broken bonds at the surface). The interaction parameter V^{AB} describes the mixing energy of the binary system. $V^{AB} = 0$ corresponds to a thermodynamic ideal solution, while $V^{AB} > 0$ corresponds to phase separation and $V^{AB} < 0$ corresponds to ordering. **Figure 1(a)** presents the typical order-disorder phase diagram of the A_cB_{1-c} solid solution considering the TBIM on a fcc lattice **[39]**. Three ordered phases are observed: two $L1_2$ phases around the composition $C_A = 0.75$ (phase A_3B) and 0.25 (phase AB_3), and the $L1_0$ phase at $C_A = 0.5$ (phase AB). T_C is the critical temperature of the order-disorder transition of the phase $L1_0$. **Figure 1(b)** shows the atomic ordering corresponding to the two binary phases $L1_0$ and $L1_2$. The TBIM was originally used considering constant atomic pair energies **[39]**. In this case, the binary system exhibits symmetric phase enthalpies and symmetric solubilities around the 50% composition, as shown in **figure 1(a)**. However, it can also be used considering atomic pair energy variations with composition, leading to asymmetric phase diagrams **[40]**. In our case, an additional element is considered noted D for example, extending TBIM considerations to a ternary system allowing the formation of a single ternary compound with the stoichiometry $A_2B_2D_4$ in addition to the binary phases, with $V^{AD} = V^{BD} < V^{AB} < 0$ (**figure 1(b)**).

In the framework of our model ternary system, the ordered phases are considered to be crystalline compounds (noted c- A_3B , c- AB , and c- AB_3), the order-disorder transition is used to

simulate the solid-liquid transition by setting the order-disorder transition temperature to the melting temperature of the corresponding ordered compound ($T_C = T_m$), and disordered (i.e. random) solutions correspond to the amorphous state (noted a-AB for example) below T_C and to the liquid state (noted liq-AB for example) above T_C . Three elements Ge, Sb, and Te, as well as three binary phase diagrams Ge-Te, Sb-Te and Ge-Sb need to be considered in the case of the GST* model. Pure element pair interactions $\varepsilon^{\text{GeGe}}$, $\varepsilon^{\text{SbSb}}$, and $\varepsilon^{\text{TeTe}}$ were determined considering the experimental cohesive energies of the pure elements ($E_{\text{coh}}(\text{Ge}) = -3.84$ eV, $E_{\text{coh}}(\text{Sb}) = -2.76$ eV, $E_{\text{coh}}(\text{Te}) = -2.22$ eV [42]) and the number of first neighbors ($Z = 12$) in the fcc lattice, while the interaction parameters V^{AB} were adjusted in order to match the T_C of the A-B phases with the T_m of the corresponding experimental A-B phases. The experimental Ge-Te, Sb-Te and Ge-Sb phase diagrams were simplified to binary phase diagrams similar to that presented in figure 1(a). Temperature-dependent allotropic transitions were neglected. Thus, the Ge-Te phase diagram is considered to possess a single phase, the GeTe compound, exhibiting a melting temperature $T_m \sim 1000$ K corresponding to the high temperature phase β -GeTe [43]. The GeTe phase was modeled by the L1₀ phase in the phase diagram presented in Figure 1(a), and in order to prevent the formation of the L1₂ phases in the TBIM Ge-Te phase diagram, the parameter V^{GeTe} was set to $V^{\text{GeTe}} = -0.095$ eV for $0.3 \leq C_{\text{Te}} \leq 0.7$ (order tendency between the two red arrows in figure 1(a)) and to $V^{\text{GeTe}} = +0.105$ eV for $C_{\text{Te}} < 0.3$ or $C_{\text{Te}} > 0.7$ (phase separation outside the two red arrows in figure 1(a)). $V^{\text{GeTe}} = -0.095$ eV allows the order-disorder transition corresponding to the transition c-GeTe/liq-GeTe to occur at $T_C \sim 1000$ K. Figure 1(d) presents the fraction of atoms ordered according to the GeTe phase versus temperature in a simulation cell containing 50% of Ge and Te atoms. One should note that atomic ordering (figure 1(b)) can be oriented according to different variants in the 3D simulation cell [39]. Consequently, phase detection was achieved at

the atomic scale, by determining if each single atom in the simulation cell belongs to one of the considered ordered phases, using an order criterion based on the number of each type of neighbors Ge, Sb, and Te, calculated up to the second neighbors of the considered atom. The phase fraction given for each phase corresponds to the fraction of atoms in the simulation cell strictly ordered according to the considered phase. Due to the 3D aspect of ordering in the simulation cell, the volume of a single phase is generally composed of numerous domains ordered according to different directions, leading to the existence of boundaries between these domains [39]. The atoms located in these boundaries cannot meet the strict order criterion of the phase, and thus, are not counted in the phase fraction. This is the reason why the maximum fraction of the GeTe phase (L1₀ order) in figure 1(d) is ~ 0.6 instead of 1. Figure 1(c) shows that the solid-liquid transition temperature of our model GeTe phase agrees with experiment. The experimental Sb-Te phase diagram shows three different phases versus composition. The phases δ ($C_{\text{Te}} \sim 0.25$ and $T_m = 818$ K) and γ ($C_{\text{Te}} \sim 0.45$ and $T_m = 820$ K) are not stoichiometric, contrasting with the phase Sb_2Te_3 ($C_{\text{Te}} = 0.6$ and $T_m = 891$ K). The phases δ , γ , and Sb_2Te_3 were respectively modelled by the phases Sb_3Te (L1₂ order), SbTe (L1₀ order), and SbTe_3 (L1₂ order) in the TBIM phase diagram (figure 1(a)). In this case, T_C was chosen as the average melting temperature $T_m \sim 850$ K of the three phases δ , γ , and Sb_2Te_3 . Figure 1(e) presents the SbTe phase fraction variations versus temperature in a simulation cell containing 50% of Sb and Te atoms. The transition c-SbTe/liq-SbTe occurs at $T_C \sim 850$ K. The parameter V^{SbTe} was set to $V^{\text{SbTe}} = -0.085$ eV for $0.2 \leq C_{\text{Te}} \leq 0.8$ (order tendency between the two blue arrows in figure 1(a)) and to $V^{\text{SbTe}} = +0.105$ eV for $C_{\text{Te}} < 0.2$ or $C_{\text{Te}} > 0.8$ (phase separation outside the two blue arrows in figure 1(a)). Setting $V^{\text{SbTe}} = +0.105$ eV outside the blue arrows in figure 1(a) aims at preventing the formation of stable Sb-Te random solutions, since random solutions are interpreted as the

amorphous state in the present case. The Ge-Sb phase diagram corresponds to phase separation. V^{AB} can be determined considering the solubility limit C_{sol} of the elements in the case of phase separation binary systems according to

$$C_{sol} \sim \exp\left(\frac{-\frac{z}{2}V^{AB}}{k_B T}\right) \quad (1)$$

Considering that the Sb solubility limit in Ge is $C_{sol} \sim 10^{19} \text{ cm}^{-3}$ at $T = 1173 \text{ K}$, one obtains $V^{\text{GeSb}} = +0.14 \text{ eV}$. However, the parameter V^{GeSb} was finally set to $V^{\text{GeSb}} = +0.21 \text{ eV}$ to improve the stability of the ternary phase $\text{Ge}_2\text{Sb}_2\text{Te}_4$. As mentioned before, the Ge-Sb phase diagram corresponds to phase separation ($V^{\text{GeSb}} > 0$). However, Ge-Sb interactions need to be attractive (with $V^{\text{GeTe}} = V^{\text{SbTe}} < V^{\text{GeSb}} < 0$) in order to stabilize the ternary compound $\text{Ge}_2\text{Sb}_2\text{Te}_4$ (GST224, **figure 1(b)**) that is used to simulate the experimental GST225 phase. Consequently, the interaction parameter V^{GeSb} should vary with composition. In order to keep symmetric binary phase diagrams, as well as for sake of simplicity, atomic interaction parameters were not allowed varying continuously with composition, but were chosen to be constant in different composition domains. To this aim, two composition ratios were defined: $R_1 = C_{\text{Sb}}/(C_{\text{Sb}} + C_{\text{Ge}})$ and $R_2 = C_{\text{Te}}/(C_{\text{Sb}} + C_{\text{Ge}})$. The parameters determined so far for binary systems (i.e. $C_{\text{Sb}} = 0$ for Ge-Te, $C_{\text{Ge}} = 0$ for Sb-Te, and $C_{\text{Te}} = 0$ for Ge-Sb) were still valid in the ternary solution (i.e. if $C_{\text{Sb}} \neq 0$ and $C_{\text{Ge}} \neq 0$ and $C_{\text{Te}} \neq 0$), except if $0.4 \leq R_1 \leq 0.8$ and $0.4 \leq R_2 \leq 1.25$, as in this case the interaction parameters were set to $V^{\text{GeTe}} = V^{\text{SbTe}} = -0.135 \text{ eV}$ and $V^{\text{GeSb}} = -0.1 \text{ eV}$. **Figure 1(f)** presents the stability of GST224 versus temperature in a simulation cell containing 25% of Ge atoms, 25% of Sb atoms and 50% of Te atoms. The order-disorder transition occurs at $T_C \sim 850 \text{ K}$, which is close to the melting temperature of GST225 **[4]**.

Atomic transport in the KMC simulations was based on first-neighbor direct exchange [44, 45, 46]. Experiments showed that GrGST cycling simulations require taking into account atomic transport in four different medias: in the amorphous solid solution, in crystalline grains and in grain boundaries (GBs), as well as in the liquid solution. To date, atomic diffusivity related to the present ternary system of interest has been quantitatively determined experimentally mostly in the case of bulk self-diffusion of pure elements. Consequently, the description of kinetics in the present KMC simulations could be perfected. However, the knowledge of self-diffusion coefficients and of general diffusion concepts can be used to determine the general rules driving kinetics in GST alloys. Atomic transport in intermetallic alloys or compounds including silicides and germanides is generally mediated by vacancies [47], which is also true in pure Ge [48, 49]. In this case, self-diffusion scales with melting temperature, and substitutional impurity diffusion is usually similar to self-diffusion [50]. In this frame, considering crystalline Ge-Sb-Te alloys, the atomic diffusivity can be set to depends on the alloy composition, following a simple proportional law between element concentrations and corresponding self-diffusion coefficients. In this case, diffusion kinetics does not depend on the diffusing specie, but on the composition of the matrix from which depends the equilibrium vacancy concentration and the melting temperature. Figure 1(c) presents self-diffusion coefficients measured (solid lines) in Ge [48], Sb [51], and Te bulk [52]. Two different coefficients ($D_{//}$ and D_{\perp}) are given for Sb and Te, since the atomic structure of these elements is not cubic, and diffusion is consequently not isotropic compared to the c-axis of their structure. Te possesses the fastest self-diffusion coefficient and its diffusion anisotropy can be neglected. The diffusion anisotropy in Sb is large, but the Sb self-diffusion activation energy in the fastest direction ($D_b^{Sb} = 0.1 \exp(-1.55 \text{ eV}/k_B T) \text{ cm}^2 \text{ s}^{-1}$) is similar to that of Te self-diffusion in the direction parallel to its c-axis ($D_b^{Te} = 0.6 \exp(-1.53$

eV/ $k_B T$) $\text{cm}^2 \text{s}^{-1}$). Consequently, the KMC diffusivity in pure Te was chosen to be equal to the experimental Te self-diffusion coefficient $D_b^{Te}{}_{KMC} = D_b^{Te}$, and the KMC diffusivity in pure Sb was chosen to correspond to the experimental D_b^{Sb} with a corrected activation energy corresponding to the activation energy of $D_b^{Te}{}_{KMC}$, giving $D_b^{Sb}{}_{KMC} = 0.1 \exp(-1.53 \text{ eV}/k_B T) \text{ cm}^2 \text{s}^{-1}$ (blue dash-line in Fig. 1c). Ge self-diffusion $D_b^{Ge} = 13.6 \exp(-3.09 \text{ eV}/k_B T) \text{ cm}^2 \text{s}^{-1}$ (red solid-line in figure 1(c)) can be more than 7 orders of magnitude slower than that of Te and Sb depending on temperature. Such a high level of difference between diffusivities cannot be considered in KMC simulations, since it would result in preventing any atomic transport in pure Ge during simulation. Generally, the maximum difference between the diffusivities of the fastest and the slowest species in atomistic KMC simulations should not exceed three to four orders of magnitude, in order to severely limit the atomic jump frequency of the slowest element without completely preventing it. Thus, the KMC diffusivity in pure Ge was chosen such as $D_b^{Ge}{}_{KMC} = D_b^{Te}{}_{KMC} / 1000 = 4 \times 10^{-3} \exp(-1.53 \text{ eV}/k_B T) \text{ cm}^2 \text{s}^{-1}$ (red dash-line in figure 1(c)). According to these kinetic considerations, the bulk diffusivity can be expressed versus composition in the KMC model as

$$D_b^{KMC} = (C_{Ge}D_0^{Ge} + C_{Sb}D_0^{Sb} + C_{Te}D_0^{Te}) \exp(-1.53 \text{ eV}/k_B T) \text{ cm}^2 \text{s}^{-1} \quad (2)$$

With C_{Ge} , C_{Sb} , and C_{Te} the respective Ge, Sb, and Te alloy composition ($C_{Ge} + C_{Sb} + C_{Te} = 1$), and $D_0^{Ge} = 4 \times 10^{-3}$, $D_0^{Sb} = 0.1$, and $D_0^{Te} = 0.6$ the prefactors of Ge, Sb, and Te self-diffusion coefficients. Atomic exchanges during KMC simulations were performed considering the frequency $\nu = D_b^{KMC}/a^2 \text{ s}^{-1}$ with $a = 0.6 \text{ nm}$ the fcc lattice parameter, and a probability of exchange $P = 1/2 \nu/\nu_{Te}$. Diffusion asymmetries are independent of temperature in this scheme, as

shown in [figure 1\(c\)](#). The fastest exchange frequency in pure Te corresponds to the exchange probability $P_{Te} = 1/2$, the slowest frequency in Ge corresponds to $P_{Ge} = 0.0033$, while $P_{Sb} = 0.083$ and $P_{224} = 0.291$, for example. This description allows a pondered Metropolis algorithm to be used, promoting fast calculations: i) a couple of first-neighbor atoms are randomly chosen, ii) the energy difference ΔU related to their lattice site exchange is calculated, iii) if $\Delta U \leq 0$ then $P = 1/2$ $(C_{Ge}D_0^{Ge} + C_{Sb}D_0^{Sb} + C_{Te}D_0^{Te})/D_0^{Te}$ or if $\Delta U > 0$ then $P = 1/2 (C_{Ge}D_0^{Ge} + C_{Sb}D_0^{Sb} + C_{Te}D_0^{Te})/D_0^{Te} \times \exp(-\Delta U/k_B T)$. If the atomic exchange is accepted, the simulation time (t) is incremented of $dt = 1/\nu$. ΔU as well as D_b^{KMC} are determined considering the local composition surrounding the two atoms considered for the exchange, calculated up to their first-neighbors. The choice of atomic transport kinetic variations versus composition is based on experimental self-diffusion coefficients measured in the crystalline phases Ge, Sb, and Te, and thus, should be fairly valid in crystalline GST phases, which correspond to the pure elements (i.e. Ge, Sb, and Te) as well as to the ordered phases (i.e. GeTe, Sb₃Te, SbTe, SbTe₃, and Ge₂Sb₂Te₄) in the simulations. However, the diffusion kinetics in GBs and in the amorphous solid solutions should be also considered. GBs are modeled in the simulation cell as the boundaries between the ordered domains. For example, [figure \(2\)](#) presents the GST224 phase fraction variations versus time during annealing of a random solution containing 25% of Ge, 25% of Sb, and 50% of Te atoms at 673 K. The simulation corresponds to the crystallization of the GST224 phase in bulk (infinite border conditions in each direction of the $20 \times 20 \times 5 \text{ nm}^3$ cell) from an amorphous solid solution a-GST224. The insert shows the Ge (red), Sb (black), and Te (white) atoms organized according to the GST224 phase at the end of the simulation. Numerous domains ordered in different directions can be observed, as well as their boundaries, where atoms are considered as being randomly distributed. GB diffusion is known as being about four orders of magnitude faster than in bulk

[^{53, 54}], and can occur at temperatures as low as 400 K [⁵⁵]. GST225 crystallization occurring at $T_x^{225} \sim 423$ K [⁴], and Ge/GST225 phase separation being initiated in the amorphous phase [^{13, 14}], atomic transport kinetics in the GrGST amorphous state appears to be several orders of magnitude faster than in crystal bulk, occurring at a similar temperature range as GB diffusion. Thus, atom transport kinetics was considered to be similar in GBs and in amorphous solid solutions in the KMC simulations by setting the diffusion coefficient in disordered solutions D_{rdm}^{KMC} such as $D_{rdm}^{KMC} = D_b^{KMC} \times 10^4$. This way, atomic transport kinetics is four orders of magnitude faster in the amorphous state and in GBs than in the corresponding crystalline phase, but diffusion kinetics scales with composition according to the same law in amorphous and crystalline states. For example, the crystallization of GST224 with (blue open circles) and without (red solid squares) considering faster diffusion in GBs and in the amorphous solution is presented in figure 2. One can note that the GST224 crystallization ends (i.e. reaches the maximum order fraction) after a shorter annealing time (~ 3 times faster) if a higher mobility is considered in GBs and in the amorphous solution. The crystallization curves are also different between the two cases, showing the influence of kinetics on grain growth (grains reorientation and grain coalescence) considering or not faster diffusion in disordered solutions.

Experiments showed that GrGST thin films crystallize into the metastable fcc-GST225 phase that carries a disorder character, contains several percent of vacancies, and that probably accepts a non-negligible off-stoichiometry degree. Different distribution of vacancies within the structure of GST225 was shown to result in different metastable GST225 structure, leading to possible off-stoichiometric metastable polymorphic GST225 structures exhibiting local chemical disorder [^{1, 28, 56}]. Furthermore, the degree of structural order in fcc-GST225 was shown to increase with temperature, while the composition disorder decreases before the fcc-GST225/hcp-

GST225 transition [1]. Consequently, it is important to consider that the GST phase may not correspond to a stoichiometric compound. Thus, two GST224 phases were considered in the KMC simulations: the stoichiometric GST224, as well as the off-stoichiometric phase off-GST224, for which a single first-neighbor atom for each considered atom was allowed to be different from the strict 224 order, corresponding to an off-stoichiometry of $\sim 15\%$, and introducing a disorder character to the phase.

In summary, the order-disorder transition on a rigid fcc lattice was used to model the amorphous-crystalline and the solid-liquid transitions in a simplified Ge, Sb, Te ternary system. The phase diagrams were simplified but still consider the same number of phases in addition to the pure phases Ge, Sb and Te: one binary phase for the Ge-Te system and three binary phases for the Sb-Te system, as well as a ternary GST phase that can exhibit an off-stoichiometry up to 15%. Thermodynamic and kinetics parameters were set to correspond to the experimental data of the ternary system Ge, Sb, Te (cohesive energies, melting temperatures, self-diffusion coefficients) considering the ternary phase GST225. Energy and kinetics depends on the local composition both in the amorphous state (random solid solutions) and the crystalline state (ordered compounds). The diffusion asymmetry is independent of temperature, and is the same in crystalline phases, GBs, and amorphous solid solutions. However, atomic transport kinetics is four orders of magnitude faster in GBs and in amorphous solid solutions.

4. Results and discussion

4.1. Influence of Ge concentration on GST crystallization

Figure 3 presents XRD in situ measurements performed on the GrGST films with $E_x = 23\%$ and $E_x = 49\%$ during the ramp annealing. The diffraction angle acquisition window ($26^\circ \leq$

$2\theta \leq 30.5^\circ$) was minimized in order to minimize XRD acquisition time, but was set such as both the Ge(111) ($2\theta \sim 27.28^\circ$) and the fcc-GST225(200) ($2\theta \sim 29.67^\circ$) diffraction peaks exhibiting maximum intensity were included in the 2θ scan range. **Figure 3** shows that crystalline Ge was not detected up to 630 K for $E_x = 23\%$, while Ge crystallization is observed at $T \sim 597$ K for $E_x = 49\%$. Considering that XRD integrated intensity is proportional to the diffracting volume of the considered phase, in situ XRD allows the relative volume variations of the crystalline phases to be observed. The presented integrated XRD intensities were normalized to the maximum intensity recorded during annealing. **Figure 4(a)** presents the integrated intensities of the fcc-GST225(200) diffraction peak versus temperature recorded during the ramp annealing of the five samples. As expected **[7,8]**, a significant shift of the GST225 crystallization temperature towards the higher temperatures is observed with the increase of Ge excess. **Figure 4(b)** shows T_x variations versus Ge excess. T_x increases linearly with E_x for $20\% \leq E_x \leq 50\%$ following the law $T_x = 387.73 + 4.1 \times E_x$. A linear behavior was already reported in the literature versus Ge concentration **[7,8]**. However, the crystallization temperature shift reaches a maximum at $E_x = 49\%$ in our case, since the two films corresponding to $E_x = 49\%$ and 61% crystallize at the same temperature: $T_x \sim 592$ K. This temperature is lower than that reported by other authors **[7,8]**, but can be explained by surface oxidation **[6]**. Indeed, our GrGST layers were not capped by a protection layer preventing oxidation. Indeed, the GST225 layer ($E_x = 0\%$) crystallized at $T_x \sim 394$ K, which is lower than the GST225 crystallization temperature without surface oxidation, $T_x \sim 443$ K for GST225 films protected by a TiN **[6]** layer for example.

Figure 5 presents the integrated XRD intensity variations of the Ge and the GST225 diffraction peaks during the ramp annealing. GST225 crystallizes before Ge in the films with low Ge excess. Ge crystallization was not observed for the GrGST film with $E_x = 23\%$ (**figure 3(a)**)

and $\Delta T_x = 50$ K between GST225 and Ge in the film with $E_x = 42\%$. However, the crystallization temperatures of Ge and GST225 converge if the Ge excess increases in the film: $\Delta T_x \sim 5$ K in the film with $E_x = 49\%$ that is close to the temperature measurement error, and $\Delta T_x = 0$ K in the film with $E_x = 61\%$ (figure 5). This trend is in agreement with the literature, however Ge was reported to crystallize before GST225 for high Ge concentrations [14,57].

Figure 6 displays the integrated XRD intensity variations of the GST225 diffraction peak, as well as the GST225 average grain size L determined from the full width at half maximum (FWHM) of the XRD peak using the Scherrer equation [58] (neglecting micro-strain), during isothermal annealing for $E_x = 0\%$ (figure 6(a)) and $E_x = 42\%$ (figure 6(b)). The grain size seems to be almost constant ($L \sim 11$ nm) at the GST225 growth beginning up to the time $t \sim 8 \times 10^3$ s, while the XRD peak intensity increases almost linearly with time in the GST225 film (figure 6(a)). This behavior is in agreement with a nucleation regime: the phase volume increases mainly due to the increase of the number of grains. After this stage, the grain size increase is proportional to the XRD peak intensity increase, which corresponds to a growth regime. The nucleation stage ended and the phase volume increases due to the increase of grain size. The GST225 grain size is about 14 nm at the end of the growth (maximum diffraction intensity), which is significantly smaller than the film thickness (200 nm). The GST225 growth kinetic is different in the GrGST film (figure 6(b)): the growth is abrupt, the maximum XRD intensity is reached in ~ 150 seconds. The nucleation stage is not observed as L follows closely the XRD intensity, meaning that GST225 growth is mainly due to grain growth. The GST225 grain size reaches rapidly 30 nm, which is the double of the grain size reached in the GST225 film ($E_x = 0\%$). Isothermal annealing was performed at higher temperature for the GrGST films ($T = 578 \pm 5$ K) than for the GST225 film ($T = 378 \pm 5$ K) due to the T_x shift in the GrGST films. Consequently, the apparent

abruptness of GST225 growth in the GrGST films could be attributed to a faster kinetics due to the temperature difference. However, GST225 was observed to form at the same temperature in the GrGST films with $E_x = 49\%$ and $E_x = 61\%$ during ramp annealing (figure 4(a)). Furthermore, figure 7 shows that GST225 forms after the same annealing time in these two samples during isothermal annealing at $T = 578$ K, but GST225 growth is less abrupt in the GrGST film with the lower Ge excess. The GST225 growth time is about 25 times longer in the GrGST film with $E_x = 49\%$ than in the film with $E_x = 61\%$. The GST225 grain size was found to be respectively $L \sim 26$ nm and $L \sim 21$ nm in the films with $E_x = 49\%$ and $E_x = 61\%$ at the end of the growth. The temperature effect on growth kinetics is similar in these two films during isotherm annealing. Thus, only the difference of Ge content can explain the observed growth kinetic difference in this case.

In summary, in situ XRD measurements during ramp annealing confirm the observations reported in the literature: GST225 crystallization temperature increases with the increase of Ge excess following a linear behavior, and Ge and GST225 crystallization temperatures converge when Ge excess increases, Ge being expected to form before GST225 in GrGST films with extremely high Ge contents. In situ isothermal annealing shows that the GST225 growth process is different in the GST225 film ($E_x = 0$) and in the GrGST films ($E_x > 20\%$). GST225 growth follows the classical nucleation and growth stages if $E_x = 0$, with almost a linear growth during nucleation and a more parabolic growth during grain growth [39, 59, 60]. In contrast, the GST225 growth is sudden in the GrGST films. The nucleation stage is not observable and the grain growth reaches rapidly a maximum. The amorphous-crystal transition seems to be faster, and the growth rate increases with Ge excess.

4.2. KMC simulations of GST crystallization

The KMC simulations were performed for bulk using different simulation cell sizes and for a 50 nm-thick film. Bulk crystallization was simulated using infinite border conditions in the three spatial directions (x, y, z) either using a $12 \times 12 \times 12 \text{ nm}^3$ cell or a $5 \times 20 \times 20 \text{ nm}^3$ cell. GST crystallization in a 50 nm-thick film was performed using a $5 \times 10 \times 50 \text{ nm}^3$ simulation cell. Infinite border conditions were used only in the x and y directions in this case, in order to consider two free surfaces in the z direction (50 nm), at the top and bottom of the film. The goal is to simulate GST crystallization versus Ge excess and to compare the results with experiments, in order to estimate the simulation relevance. The KMC time increment dt being not constant, since it depends on atomic exchanges that depend on local composition, ramp annealing were not simulated. Isothermal annealing was simulated at $T = 673 \text{ K}$ for four different Ge excess, i) $E_x = 0$ (224 stoichiometry: 25 at% Ge, 25 at% Sb, and 50 at% Te), ii) $E_x = 20\%$ (40 at% Ge, 20 at% Sb, and 40 at% Te), iii) $E_x = 40\%$ (55 at% Ge, 15 at% Sb, and 30 at% Te), and iv) $E_x = 60\%$ (70 at% Ge, 10 at% Sb, and 20 at% Te). No significant differences were observed between the results obtain in the different simulation cells in bulk or thin film. For example, [figures 8\(a\) and 8\(b\)](#) present the phase distributions in bulk and thin film before and after the formation of GST224 if $E_x = 60\%$. Ge (red atoms) formation is followed by the rapid formation of the phase off-GST224 (black atoms) in the two cases. The bulk microstructure is similar to the film microstructure: small off-GST224 grains are surrounded by Ge. The two images of the simulation cell before and after the formation of off-GST224 are separated by 0.22 s in [figure 8\(a\)](#) and by 0.62 s in [figure 8\(b\)](#). Stoichiometric GST224 does not form even after an annealing time $t_A > 8$ minutes.

[Figure 4\(c\)](#) presents the total GST224 phase fraction variations (= GST224 + off-GST224 phase fractions) versus annealing time during isothermal annealing for the four films with different Ge excess ($E_x = 0, 20, 40$, and 60%), and [figure 4\(d\)](#) the nucleation time for GST224.

The GST224 nucleation time t_x increases with Ge excess. This behavior is in agreement with the T_x increase observed experimentally with Ge excess during the ramp annealing (figure 4(a)). However, t_x is found to vary exponentially with Ge excess (figure 4(d)), while T_x was found following a linear behavior versus Ge excess (figure 4(b)).

Figure 9 shows the Ge and the total GST224 normalized phase fraction variations during isothermal annealing for the three GrGST films with $E_x = 20\%$ (figure 9(a)), $E_x = 40\%$ (figure 9(b)), and $E_x = 60\%$ (figure 9(c)). Ge and GST224 crystallize almost simultaneously in the film with $E_x = 20\%$, while Ge crystallization occurs before GST224 crystallization in the films with $E_x = 40$ and 60% , the crystallization time difference between Ge and GST224 increasing with Ge excess. This behavior is in agreement with the experimental trend presented in figure 5 and with the observations reported in the literature [7, 8, 14, 57] during ramp annealing.

Stoichiometric GST224 crystallization in bulk (open circles in figure 2) and in film (open squares in figure 4(c)) occurs following the classical nucleation and growth processes. However, this is not the case of off-GST224 crystallization. For example, figures 8(c) and 8(d) present the phase fraction variations of the phases detected in the simulation cell versus time during isothermal annealing of bulk GrGST with $E_x = 20$ and 40% . GST224 (solid circles) is the first phase to form if $E_x = 20\%$. Its growth is continuous and needs ~ 1 s to reach a maximum phase fraction ~ 0.1 (figure 8(c)). off-GST224 crystallization (solid up-triangles) occurs after GST224, but its growth is extremely fast, off-GST224 reaching a phase fraction ~ 0.6 in ~ 0.07 s, before that GST224 can reach its maximum phase fraction. The simulation cell before off-GST224 formation shows randomly distributed GST224 grains (white atoms), corresponding to the classical scheme of random nucleation followed by growth. In contrast, off-GST224 (black atoms) is found to be fully distributed in the entire simulation cell in less than 0.07 s. Ge forms after GST224 and its phase fraction stays very small. The phase formation sequence is

significantly modified in the case of the GrGST film with $E_x = 40\%$ (figure 8(d)): Ge is the first phase to form, and is followed by the crystallization of off-GST224 after a time $t_x \sim 1$ s. Finally, GST224 is the last phase to crystallize after a time $t_x > 6$ s. One can note that off-GST224 formation is again sudden, and does not involve a significant discharge of Ge, as the Ge phase fraction is not modified by the abrupt formation of off-GST224. The Ge phase fraction stays constant up to the formation of GST224 that leads in this case to a significant discharge of Ge. The delay of GST224 crystallization due to the increase of Ge excess leads to the simultaneous increase of the total GST224 and of the Ge phase fractions, after that the total GST224 fraction has already reached a first plateau. In this case, the simulation cell before off-GST224 formation shows only Ge (red atoms), with a distribution corresponding to randomly distributed Ge grains that started to coalesce after nucleation and growth. The formation of off-GST224 is again characterized by the simultaneous apparition of the phase in the entire simulation cell. The difference of growth kinetics between Ge and off-GST225 is also illustrated in figure 9(c). No GST224 grains are observed at that time. However, the two images (Fig. 8(d), the large one displays all the phases: Ge, off-GST224, and GST224, while the smaller displays only Ge and GST224 for clarity) of the same simulation cell after annealing for 30 s show the GST224 grains that have grown later. The GST224 domains exhibit a concentration gradient leading to a pseudo core-shell structure. The core matches the 224 stoichiometry, while the shell corresponds to off-GST224. The GST224 domains are surrounded by the Ge matrix. The simulations show that the increase of Ge excess leads simultaneously to the decrease of the GST224 phase fraction and to a delay of its crystallization, with the concomitant increase of the off-GST224 phase fraction. When the Ge excess reaches a critical level, the GST224 ceases to form and the film is only composed of the off-GST224 phase, as illustrated in figures 8(a) and 8(b) for $E_x = 60\%$. This phenomenon is in agreement with the experimental XRD intensities shown in figure 7. Indeed,

GST225 growth kinetic in the film with $E_x = 49\%$ is in agreement with the intermediated case, for which stoichiometric GST225 still corresponds to a non-negligible volume of material and nucleates just after the formation of an off-stoichiometric GST225 phase, explaining the observation of two consecutive growth regimes with first fast kinetics and then slow kinetics. Furthermore, the increase of Ge excess up to $E_x = 61\%$ in the second film is in agreement with a strong reduction of the stoichiometric GST225 volume compared to the volume of the off-stoichiometric phase, leading to the observed abrupt formation. It is interesting to note that the behavior shown in [figure 8\(d\)](#) was actually observed experimentally during the crystallization of GeTe ^[43]: after reaching a plateau during in situ XRD measurements, the GeTe diffraction peak increases simultaneously with Ge crystallization.

The difference of growth kinetics between GST224 and off-GST224 is linked to their properties. GST224 is the stable phase exhibiting the minimum energy and possesses a strict stoichiometry. Thus, its formation requires a significant discharge of Ge to form a nucleus exhibiting the correct stoichiometry. GST224 possesses the same composition in the entire sample. In contrast, the formation of off-GST224 allows a smaller energy gain than that of GST224, but off-GST224 requires a smaller Ge discharge and its stoichiometry can vary of several percent locally in the sample. GST224 is thermodynamically favored. However, the formation of the GST224 nucleus depends on local composition and atomic transport kinetics in the amorphous solution. The fast diffusion in the amorphous solution can allow a composition matching the composition domain of off-GST224 to be reached almost simultaneously in all the film, triggering its rapid formation simultaneously in the entire sample (larger the authorized stoichiometry deviation, stronger the simultaneous effect). Consequently, larger the Ge excess, smaller the GST224 volume, and slower the GST224 nucleus formation, supporting the formation of off-GST224.

The formation of off-GST224 requires less Ge discharge and is controlled by atomic transport kinetics in the amorphous solid solution. Consequently, Ge excess should lead to two opposite effects: i) off-GST224 should form before stoichiometric GST224, as it needs to discharge less Ge, which should decrease T_x compared to GST224, but ii) increasing Ge concentration decreases atomic transport kinetics in the amorphous matrix and thus delays off-GST224 formation, leading to an increase of T_x . The simulations and the experiments show that Ge excess leads to an increase of T_x . This is due to the fact that the stoichiometric phase is stable only in a small concentration domain. Increasing Ge concentration reduces its stability, the fraction of GST224 decreases and its formation is delayed due to the necessity to reach the correct stoichiometry by discharging more Ge. Off-GST224 forms before GST224 in this case, but GST224 volume becomes negligible compared to the volume of off-GST224 as shown in [figure 8\(d\)](#). T_x becomes only dependent on the formation of off-GST224, which depends on self-diffusion in the amorphous solid solution. This dependency is illustrated in [figure 4\(d\)](#), where t_x is shown to vary exponentially with Ge excess. It is interesting to note that the simulations suggest that Ge excess should lead to both an increase of T_x and an increase of the switching time linked to the amorphous-crystalline transition. Furthermore, the introduction in the matrix of any impurity modifying atomic transport kinetics in the amorphous solid solution should modify T_x .

In summary, simulation of GST thin film crystallization using the simplified ternary GST* system allows several experimental observations to be qualitatively reproduced: T_x (or t_x) increases with Ge excess; Ge formation occurs after GST formation for low Ge excess, while it tends to occur before that of GST for high Ge excess; and GST growth kinetic variations versus Ge excess similar to experiments are observed in the simulations. The similarities between experiment and simulation are resulting from the possible formation of a non-stoichiometric GST phase exhibiting the same atomic lattice structure as the stoichiometric GST compound.

4.3. KMC simulation of GST Set/Reset cycling

This part aims at simulating sequential SET and RESET operations performed on a 50 nm-thick film using the GST^{*} model, considering heating the film with a heat source located at the bottom of the film, such as in the case of GST memory cells heated with a Heater element. The film (or the memory cell) is subjected to a temperature gradient in this case, allowing the material at the bottom of the film to be molten, while keeping the solid state at the top of the film during RESET, for example. This is not easily performed experimentally, justifying the use of simulations, and is very close to the case of a memory cell, but requires a reduced number of atoms in the simulation cell. **Figure 10** presents the temperature distributions used during the SET and RESET operations. The temperature was assumed to be homogeneous in the thickness of the film during the SET, with $T = 673$ K. This temperature was chosen as it is high enough to promote rapid crystallization of GST224, but is 177 K below the melting temperature of GST224. The same temperature was used in section 4.2 in order to evaluate the influence of the temperature gradient on the atomic distribution during RESET by comparing the cycling results with the case of GST crystallization in isothermal experimental conditions. The temperature distribution was assumed to follow a Gaussian distribution during RESET from the bottom of the film up to its midsection, reaching then the constant temperature $T = 673$ K up to the top of the film. Diffusion coefficients in liquid metals are usually of the order of $\sim 5 \times 10^{-5} \text{ cm}^2 \text{ s}^{-1}$ [61], and Ge self-diffusion in liquid Ge at its melting temperature is $\sim 1.3 \times 10^{-4} \text{ cm}^2 \text{ s}^{-1}$ [62]. Consequently, the maximum temperature of the RESET was chosen to be artificially extremely high in order to simulate the atomic transport kinetic in the melted region. Two RESET temperatures were used $T = 2000$ K for the so called RESET 1 with a Ge self-diffusion

coefficient $\sim 5.6 \times 10^{-7} \text{ cm}^2 \text{ s}^{-1}$, and $T = 4000 \text{ K}$ for the so called RESET 2 with a Ge self-diffusion coefficient $\sim 2.4 \times 10^{-3} \text{ cm}^2 \text{ s}^{-1}$. RESET 1 corresponds to a diffusion kinetic below Ge self-diffusion in liquid Ge, and RESET 2 corresponds to a diffusion kinetic above Ge self-diffusion in liquid Ge at its melting temperature ($\sim 1213 \text{ K}$). The annealing time was set to one minute for both SET and RESET. This is several orders of magnitude longer than that of real SET and RESET operations used to switch memory cells. The use of a longer operation time aims at accelerating the cycling in order to converge faster to the enduring atomic distribution using a limited number of cycles. Furthermore, KMC simulations being based on a pondered Metropolis algorithm, the sequence of atomic exchanges should provide quantitative information on the atomic distribution evolution of the considered system. However, the time scale should not be considered as quantitative information, in particular since experimental atomic transport kinetics is not known in the amorphous solid solution, and thus, could not be used to parameter the simulations. The simulations of GrGST thin films crystallization during isothermal annealing showed that stoichiometric GST224 cannot form for large Ge excess. Thus, the cycling simulations were performed for thin films with $E_x = 40\%$, since it allows the case of stoichiometric GST224 as well as the case of non-stoichiometric GST224 to be investigated, and to compare the obtained microstructures. One reason of GrGST memory failure was suggested to be related to the formation of Ge grains in contact with the electrodes. Thus, the effect of a GST224 seed localized at the bottom of the film (bottom electrode) or both at the bottom and at the top of the film (top electrode) was investigated. The GST seed corresponds to a 10 nm-thick amorphous layer (i.e. random solution) with the 224 stoichiometry deposited either before the GrGST layer (bottom seed) or after the GrGST layer (top seed). Five cycles of consecutive SET and RESET were simulated. For example, [figure 11\(a\)](#) presents the evolution of the film

microstructure for the entire five SET/RESET cycles using RESET 1 in the case of stoichiometric GST224 without seed (red, white, and black atoms belongs to the phases Ge, GST224, and off-GST224, respectively).

4.3.1 Stoichiometric GST

Figure 11(a) shows that, during cycling with RESET 1, the microstructure changes from a random distribution of GST224 grains surrounded by Ge (GST-cluster structure) to a multilayer Ge/GST structure parallel to the film surface (GST-band structure) in the case of stoichiometric GST224. The last SET (SET/RESET V) led to the formation of a thin Ge layer on top of the film, but the bottom of the film (Heater side) is made of a GST224 layer. The microstructure at the top of the film stays the same after RESET, but the bottom part of the film corresponding to the GST224 layer is entirely amorphous. The structure of the film does not drastically change after the third cycle, the SET/RESET operations leading to sequential crystallization/amorphization of the bottom GST224 layer. Same results were obtained with RESET 2, the significant increase of atomic mobility in the melted bottom part of the film during RESET has no significant effects on the microstructure. Furthermore, the same GST-band structure was observed after long-time isothermal annealing (> 30 minutes). However, the top and the bottom of the film are both made of a Ge layer in this case. High atomic mobility at the Heater side appears to favor the formation of GST224.

Figure 12 illustrates the effect of the seed layers, showing the simulation cells for the fifth SET and RESET of both RESET 1 (**figures 12(a)** and **12(c)**) and RESET 2 (**figures 12(b)** and **12(d)**). The evolution of the microstructure leads again towards the GST-band structure. The use of a seed layer at the bottom of the film does not change the SET microstructure at that location, since a GST224 layer is located close to the heater, as in the case without seed. However, the

bottom seed leads to an increase of the GST224 volume in the film, modifying the microstructure at the top of the film, where the main part of Ge tends to gather. The use of a second seed at the top of the film allows the top electrode to be in contact with a GST224 layer instead of Ge. The use of the two seeds forces the Ge layers to be located inside the volume of the film and provide GST224 layers in contact with the two electrodes after SET. The RESET leads to the amorphization of the bottom part of the film that keeps the 224 stoichiometry, allowing GST224 to form at this location after each SET. RESET 1 and RESET 2 lead to similar results, as well as long-time isothermal annealing at $T = 673$ K.

Figures 12(e) shows a simple schematic illustrating the structure modification from the GST-cluster structure to the GST-band structure with cycling. Ge and GST volumes are considered to be preserved during the structure evolution (mass conservation). According to this schematic, the GST-cluster structure can be modeled with two different parallel electrical resistances R_I (through Ge) and R_{II} (through alternating Ge and GST volumes), while $R_I = R_{II}$ for the GST-band structure. Assuming for simplification that the Ge resistance is about the same as the GST resistance if the film is entirely amorphous ($R_{aGe} \sim R_{aGST}$), and that the Ge resistance is significantly higher than the GST resistance if the film is entirely crystalline ($R_{cGe} \gg R_{cGST}$), one can show that $\Delta R_{bd} \sim \frac{3}{4} \Delta R_{cl}$, with ΔR_{cl} and ΔR_{bd} the film resistance variation between the crystalline and amorphous states for the GST-cluster structure and the GST-band structure, respectively. Consequently, the structure evolution observed during cycling in the case of a stoichiometric GST is expected to lead to a decrease of the memory cell programming window.

In summary, in the case of a stoichiometric GST, cycling leads to the same microstructure in the GrGST film as long-time isothermal annealing after SET, which is characterized by the formation of a Ge/GST multilayer structure. However, the multilayer structure starts with a Ge

layer at the bottom of the film and ends also with a Ge layer at the top of the film in the case of isothermal annealing, while the temperature gradient used during cycling favors the formation of a GST layer on the side of the film in contact with the Heater (hotter side). This structure is independent of large temperature variations in the melted region during RESET. The use of a seed layer on top of the film (colder side) should prevent the formation of a Ge layer in contact with the upper electrode. The formation of the multilayer structure during annealing or cycling is expected to lead to a decrease of the memory cell programming window.

4.3.2 Non-stoichiometric GST

The microstructure evolution of the non-stoichiometric GST is different from the case of stoichiometric GST. For example, [figure 11\(b\)](#) shows the evolution of the film microstructure for non-stoichiometric GST with a bottom seed using RESET 1. The images of the SET and RESET stages are doubled for clarity, one image showing all the detected phases and a second omitting the phase off-GST224. Isothermal annealing showed that the initial crystallization microstructure in the GrGST film is the same for GST224 and for off-GST224, corresponding to a GST-cluster structure. But the GST224 microstructure changes to the GST-band structure with time, while off-GST224 stabilizes the GST-cluster structure. During cycling, the GST-cluster structure is quicker destabilized to form the GST-band structure if GST224 is stoichiometric, but the GST-cluster structure is still stabilized if GST224 is non-stoichiometric. [Figure 13](#) presents the microstructure of the film after the last SET and RESET for RESET 1 and RESET 2 for non-stoichiometric GST. Off-GST224 stabilizes the GST-cluster structure in the two cases, but the microstructure of the film is different with the different RESET, showing the influence of the temperature distribution and of the diffusion kinetics in the liquid solution on the SET microstructure. In particular, Ge is more redistributed during RESET if atomic mobility in the

melted region is higher (RESET 2). GST224 is separated from Ge by off-GST224 after SET, as well as in the crystalline part of the film after RESET, which is in agreement with a decreasing Ge concentration gradient from Ge to off-GST224 and GST224. The amorphous region at the bottom of the film keeps a stoichiometry corresponding to off-GST224 after RESET, and off-GST224 is still identified despite that GST224 disappeared. The definition of off-GST224 promotes a higher incorporation of Ge as well as a disorder degree in the phase, which leads to a higher apparent stability on the rigid lattice. However, the diffusion kinetics in the bottom region of the film during RESET corresponds to that of a melted solution, and this region should be considered to be amorphous after RESET.

Figure 14 presents the influence of a seed layer on the film microstructure for both RESET 1 and RESET 2 in the case of non-stoichiometric GST224. Contrasting with the case of stoichiometric GST224, the seed layers have a strong influence on the microstructure, since it is different for the four different cases: RESET 1 with a single (figure 14(a)) or two (figure 14(c)) seed layers and RESET 2 with one (figure 14(b)) or two (figure 14(d)) seeds. The use of two seed layers at the bottom and at the top of the GrGST layer may be justified in the case of non-stoichiometric GST224, as it allows the bottom and top electrodes to be in contact with the GST instead of Ge after SET. However, the use of two seeds and RESET 1 promotes the formation of a microstructure similar to the GST-band structure observed for stoichiometric GST224 after SET, expected to reduce the memory programming window. In contrary, the use of two seeds and RESET 2 promotes a microstructure with Ge/GST multilayers oriented perpendicularly to the film surface after SET. In this case, a significant concentration gradient is observed in the film, since the top electrode is in contact with GST224 (top of the film), while the bottom electrode is in contact with off-GST224 (bottom of the film) after SET. These results show that the evolution of the film microstructure is highly dependent on atom kinetics in the melted solution as well as

on the temperature distribution in the film during RESET in the case of non-stoichiometric GST. Furthermore, the microstructure evolution is also strongly dependent on the film composition variations linked to the addition of seed layers. The thickness of the seed layers should be carefully adjusted in order to promote the desired microstructure with top and bottom electrodes in contact with GST.

In summary, isothermal and cycling annealing stabilize a GST-cluster structure in the film in the case of non-stoichiometric GST. However, contrasting with the case of stoichiometric GST, the film microstructure is highly dependent on RESET conditions as well as on the use of seed layers during cycling. Indeed, depending on RESET conditions and on the use of a single or two seed layers, the film microstructure can either tend towards a GST-cluster structure or a GST-band structure, or exhibit a quasi-multilayer structure oriented perpendicularly to the film surface.

4. Conclusion

KMC simulations were performed aiming to simulate the crystallization of GrGST films as well as SET/RESET cycling of a 50 nm-thick GrGST film. A first-neighbor-interaction TBIM description was used to define a simplified Ge-Sb-Te ternary system GST* on a rigid fcc lattice, using the order-disorder transition to model the amorphous-crystalline transition at low temperature and the solid-liquid transition at high temperature. The GST* system was parametrized with the cohesive energy of the pure elements, the average melting temperature of the binary and ternary compounds, and the self-diffusion coefficients of the pure elements. The system energy as well as atomic transport kinetics were considered to vary with local composition according to Vegard's laws, and atomic transport kinetics was considered to be

similar in the amorphous solid solution and GBs, and to be four orders of magnitude faster than in crystalline phases.

The model was shown to be in qualitative agreement with experimental observations during isothermal and ramp annealing of GrGST layers, assuming the GST ternary compound to be non-stoichiometric, or at least allowing the formation of a metastable off-stoichiometric GST phase during annealing. The influence of the nature of the GST compound (stoichiometric or non-stoichiometric), the RESET conditions, and the use of seed layers on the film microstructure were investigated during SET/RESET cycling. Isothermal crystallization of stoichiometric GST forms first a GST-cluster structure that changes into a GST-band structure with Ge localized at the top and bottom of the film. Crystallization during cycling annealing with a temperature gradient shows a similar behavior excepted that the GST is localized on the high-temperature side instead of Ge after SET. The use of a seed layer on the Heater side does not change drastically the results, but the use of a seed layer on the colder side allows the electrode on this side to be in contact with GST instead of Ge. These results are almost independent of the diffusion kinetics in the melted region close to the Heater during RESET. Contrasting with stoichiometric GST, isothermal and cycling annealing stabilize a GST-cluster structure in the case of non-stoichiometric GST. Furthermore, RESET conditions as well as the use of seed layers have a strong impact on the film microstructure after SET in this case. The cycling SET and RESET conditions (maximum temperature, temperature distribution along the gradient) as well as the location, the number and the thickness of the seed layers should be carefully determined in order to control the microstructure evolution of the film with cycling, and thus, to control the film electrical properties.

More quantitative results are expected to be obtained if the model kinetics could be described using experimental data from self-diffusion in liquid, amorphous, and crystalline

GrGST, as well as in GBs. Correct description of temperature distributions in the film during SET and RESET is also required for more quantitative results.

ACKNOWLEDGEMENTS

This project was supported by the French National Association of Research and Technology (ANRT Project 2020/0907).

REFERENCES

1. Lotnyk, A., Behrens, M. & Rauschenbach, B. Phase change thin films for non-volatile memory applications. *Nanoscale Adv.* **1**, 3836–3857 (2019).
2. Raoux, S. *et al.* Phase-change random access memory: A scalable technology. *IBM J. Res. Dev.* **52**, 465–479 (2008).
3. Burr, G. W. *et al.* Phase change memory technology. *J. Vac. Sci. Technol. B, Nanotechnol. Microelectron. Mater. Process. Meas. Phenom.* **28**, 223–262 (2010).
4. Guo, P., Sarangan, A. M. & Agha, I. A review of germanium-antimony-telluride phase change materials for non-volatile memories and optical modulators. *Appl. Sci.* **9**, (2019).
5. Putero, M. *et al.* Evidence for correlated structural and electrical changes in a Ge₂Sb₂Te₅ thin film from combined synchrotron X-ray techniques and sheet resistance measurements during in situ thermal annealing. *J. Appl. Crystallogr.* **44**, 858–864 (2011).
6. Noé, P., Vallée, C., Hippert, F., Fillot, F. & Raty, J.-Y. Phase-change materials for non-volatile memory devices: from technological challenges to materials science issues. *Semicond. Sci. Technol.* **33**, 013002 (2018).
7. Zuliani, P. *et al.* Overcoming temperature limitations in phase change memories with optimized GexSbyTez. *IEEE Trans. Electron Devices* **60**, 4020–4026 (2013).
8. Ciocchini, N. *et al.* Modeling resistance instabilities of set and reset states in phase change memory with Ge-rich GeSbTe. *IEEE Trans. Electron Devices* **61**, 2136–2144 (2014).
9. Oh, S. H. *et al.* In situ TEM observation of void formation and migration in phase change memory devices with confined nanoscale Ge₂Sb₂Te₅. *Nanoscale Adv.* **2**, 3841–3848 (2020).
10. Loke, D. *et al.* Breaking the speed limits of phase-change memory. *Science* (80-.). **336**, 1566–1569 (2012).

11. Yamada, N. & Matsunaga, T. Structure of laser-crystallized Ge₂Sb_{2+x}Te₅ sputtered thin films for use in optical memory. *J. Appl. Phys.* **88**, 7020–7028 (2000).
12. Zhang, W. *et al.* Density-functional theory guided advances in phase-change materials and memories. *MRS Bull.* **40**, 856–864 (2015).
13. Agati, M., Renaud, F., Benoit, D. & Claverie, A. In-situ transmission electron microscopy studies of the crystallization of N-doped Ge-rich GeSbTe materials. *MRS Commun.* **8**, 1145–1152 (2018).
14. Agati, M., Vallet, M., Joulié, S., Benoit, D. & Claverie, A. Chemical phase segregation during the crystallization of Ge-rich GeSbTe alloys. *J. Mater. Chem. C* **7**, 8720–8729 (2019).
15. Orava, J. & Greer, A. L. *Chalcogenides for Phase-Change Memory. Handbook of Thermal Analysis and Calorimetry* vol. 6 (Elsevier B.V., 2018).
16. Li, J. *et al.* Explore physical origins of resistance drift in phase change memory and its implication for drift-insensitive materials. *Tech. Dig. - Int. Electron Devices Meet. IEDM* 291–294 (2011) doi:10.1109/IEDM.2011.6131541.
17. Padilla, A. *et al.* Voltage polarity effects in Ge₂Sb₂Te₅-based phase change memory devices. *J. Appl. Phys.* **110**, (2011).
18. Park, J.-B. *et al.* Phase-Change Behavior of Stoichiometric Ge₂Sb₂Te₅ in Phase-Change Random Access Memory. *J. Electrochem. Soc.* **154**, H139 (2007).
19. Cheng, H. Y., Raoux, S. & Chen, Y. C. The impact of film thickness and melt-quenched phase on the phase transition characteristics of Ge₂Sb₂Te₅. *J. Appl. Phys.* **107**, (2010).
20. Micoulaut, M., Piarristeguy, A., Flores-Ruiz, H. & Pradel, A. Towards accurate models for amorphous GeTe: Crucial effect of dispersive van der Waals corrections on the structural properties involved in the phase-change mechanism. *Phys. Rev. B* **96**, (2017).

21. Lee, T. H. & Elliott, S. R. The Relation between Chemical Bonding and Ultrafast Crystal Growth. *Adv. Mater.* **29**, (2017).
22. Roohforouz, A. & Shokri, A. Subthreshold electron transport properties of ultrathin film phase change material Ge₂Sb₂Te₅. *AIP Adv.* **9**, (2019).
23. Elliott, S. & Hegedus, J. Computer simulation of the phase-change cycle of GST-225. *Mater. Res. Soc. Symp. Proc.* **1072**, 99–107 (2008).
24. Ronneberger, I., Zhang, W. & Mazzarello, R. Crystal growth of Ge₂Sb₂Te₅ at high temperatures. *MRS Commun.* **8**, 1018–1023 (2018).
25. Lee, T. H. & Elliott, S. R. Chemical Bonding in Chalcogenides: The Concept of Multicenter Hyperbonding. *Adv. Mater.* **32**, (2020).
26. Lee, T. H. & Elliott, S. R. Multi-Center Hyperbonding in Phase-Change Materials. *Phys. Status Solidi - Rapid Res. Lett.* **15**, (2021).
27. Lee, T. H. & Elliott, S. R. Ab initio computer simulation of the early stages of crystallization: Application to Ge₂Sb₂Te₅ phase-change materials. *Phys. Rev. Lett.* **107**, 1–5 (2011).
28. Zhang, W., Wuttig, M. & Mazzarello, R. Effects of stoichiometry on the transport properties of crystalline phase-change materials. *Sci. Rep.* **5**, 1–10 (2015).
29. Lencer, D. *et al.* A map for phase-change materials. *Nat. Mater.* **7**, 972–977 (2008).
30. Huang, B. & Robertson, J. Bonding origin of optical contrast in phase-change memory materials. *Phys. Rev. B - Condens. Matter Mater. Phys.* **81**, 1–4 (2010).
31. Wuttig, M., Deringer, V. L., Gonze, X., Bichara, C. & Raty, J. Y. Incipient metals: Functional materials with a unique bonding mechanism. *Adv. Mater.* **30**, 1–6 (2018).
32. Raty, J. Y. *et al.* A Quantum-Mechanical Map for Bonding and Properties in Solids. *Adv. Mater.* **31**, 1–6 (2019).

33. Siegrist, T. *et al.* Disorder-induced localization in crystalline phase-change materials. *Nat. Mater.* **10**, 202–208 (2011).
34. Edwards, A. H. *et al.* Electronic structure of intrinsic defects in crystalline germanium telluride. *Phys. Rev. B - Condens. Matter Mater. Phys.* **73**, 1–13 (2006).
35. Raty, J. Y. *et al.* Aging mechanisms in amorphous phase-change materials. *Nat. Commun.* **6**, 1–8 (2015).
36. Battaile, C. C. The Kinetic Monte Carlo method: Foundation, implementation, and application. *Comput. Methods Appl. Mech. Eng.* **197**, 3386–3398 (2008).
37. Buscemi, F., Piccinini, E., Brunetti, R., Rudan, M. & Jacoboni, C. Monte Carlo simulation of charge transport in amorphous chalcogenides. *J. Appl. Phys.* **106**, (2009).
38. Melnic, O. *et al.* Monte Carlo model of resistance evolution in embedded PCM with Ge-rich GST. *Dig. Tech. Pap. - Symp. VLSI Technol.* **2019-June**, T64–T65 (2019).
39. Portavoce, A. & Tréglia, G. Physical origin of thickness-controlled sequential phase formation during reactive diffusion: Atomistic modeling. *Phys. Rev. B - Condens. Matter Mater. Phys.* **82**, (2010).
40. Portavoce, A. & Tréglia, G. Theoretical investigation of the influence of reaction and diffusion kinetics upon thin-film reactive diffusion. *Phys. Rev. B - Condens. Matter Mater. Phys.* **85**, (2012).
41. Tréglia, G., Legrand, B. & Ducastelle, F. Segregation and ordering at surfaces of transition metal alloys: The tight-binding ising model. *Epl* **7**, 575–580 (1988).
42. Kittel, C. *Introduction to solid state physics.* (Wiley, 1996).
43. Gallard, M. *et al.* New insights into thermomechanical behavior of GeTe thin films during crystallization. *Acta Mater.* **191**, 60–69 (2020).
44. Roussel, J. M., Saúl, A., Tréglia, G. & Legrand, B. Microstructure of the surfactantlike

- effect in Ni/Ag(100) and (111). *Phys. Rev. B - Condens. Matter Mater. Phys.* **55**, 10931–10937 (1997).
45. Legrand, B., Saúl, A. & Trégliia, G. Layer-by-layer versus surfactant dissolution modes in heteroepitaxy. *Phys. Rev. B - Condens. Matter Mater. Phys.* **60**, 13890–13901 (1999).
 46. Roussel, J. M., Saúl, A., Trégliia, G. & Legrand, B. Linear time dependence of the surfactant effect: A local equilibrium under flux. *Phys. Rev. B - Condens. Matter Mater. Phys.* **69**, 1–8 (2004).
 47. Helmut, M. *Diffusion in Solids*. (Springer-Verlag, 2007).
 48. Werner, M., Mehrer, H. & Hochheimer, H. D. Effect of hydrostatic pressure, temperature, and doping on self-diffusion in germanium. *Phys. Rev. B* **32**, 3930–3937 (1985).
 49. Südkamp, T. *et al.* Doping dependence of self-diffusion in germanium and the charge states of vacancies. *Appl. Phys. Lett.* **102**, 242103 (2013).
 50. Portavoce, A. *et al.* Manganese diffusion in monocrystalline germanium. *Scr. Mater.* **67**, 269–272 (2012).
 51. Cordes, H. & Kim, K. Self-Diffusion in Antimony. *J. Appl. Phys.* **37**, 2181–2181 (1966).
 52. Werner, M., Mehrer, H. & Siethoff, H. Self-diffusion and antimony diffusion in tellurium. *J. Phys. C Solid State Phys.* **16**, 6185–6195 (1983).
 53. Portavoce, A., Chow, L. & Bernardini, J. Triple-junction contribution to diffusion in nanocrystalline Si. *Appl. Phys. Lett.* **96**, (2010).
 54. Blum, I. *et al.* Lattice and grain-boundary diffusion of As in Ni₂ Si. *J. Appl. Phys.* **104**, (2008).
 55. Portavoce, A., Hoummada, K. & Dahlem, F. Influence of interfacial reaction upon atomic diffusion studied by in situ Auger electron spectroscopy. *Surf. Sci.* **624**, (2014).
 56. Xu, M., Zhang, W., Mazzarello, R. & Wuttig, M. Disorder Control in Crystalline GeSb₂

- Te 4 Using High Pressure. *Adv. Sci.* **2**, 1500117 (2015).
57. Thomas, O. *et al.* Crystallization behavior of N -doped Ge-rich GST thin films and nanostructures: An in-situ synchrotron X-ray diffraction study. *Microelectron. Eng.* **244–246**, 111573 (2021).
 58. Holzwarth, U. & Gibson, N. The Scherrer equation versus the ‘Debye-Scherrer equation’. *Nat. Nanotechnol.* **6**, 534–534 (2011).
 59. Nemouchi, F., Mangelinck, D., Bergman, C., Gas, P. & Smith, U. Differential scanning calorimetry analysis of the linear parabolic growth of nanometric Ni silicide thin films on a Si substrate. *Appl. Phys. Lett.* **86**, 041903 (2005).
 60. Hoummada, K., Portavoce, A., Perrin-Pellegrino, C., Mangelinck, D. & Bergman, C. Differential scanning calorimetry measurements of kinetic factors involved in silicide process. *Appl. Phys. Lett.* **92**, 133109 (2008).
 61. Meyer, A., Hennig, L., Kargl, F. & Unruh, T. Iron self diffusion in liquid pure iron and iron-carbon alloys. *J. Phys. Condens. Matter* **31**, 395401 (2019).
 62. Weis, H. *et al.* Self- and interdiffusion in dilute liquid germanium-based alloys. *J. Phys. Condens. Matter* **31**, 455101 (2019).

FIGURE CAPTIONS

FIG. 1. Characteristics of the ternary GST* model: a) binary TBIM phase diagram on fcc lattice; b) atomic ordering corresponding to the binary and ternary compounds; c) Ge (red), Sb (blue), and Te (pink) self-diffusion coefficients, experiments (D) and simulations (D_{KMC}); d), e), and f) stability of the compounds GeTe, SbTe, and $\text{Ge}_2\text{Sb}_2\text{Te}_4$ versus temperature (order-disorder transition), respectively.

FIG. 2. KMC simulations of GST224 crystallization at $T = 673$ K from an amorphous solid solution with the 224 stoichiometry: variation of the GST224 volume versus annealing time. Solid squares correspond to simulations with homogeneous atomic transport kinetics, and open circles correspond to simulations considering faster atomic diffusion in both GBs and amorphous solid solutions. The insert shows the atoms belonging to the GST224 phase in the $5 \times 20 \times 20$ nm³ simulation cell (red, black, and white atoms respectively correspond to Ge, Sb, and Te) at the end of the simulation ($t = 60$ s).

FIG. 3. XRD intensity measured during in situ ramp annealing at 2K min^{-1} of a 200 nm-thick GrGST film with a) $E_x = 23\%$, and b) $E_x = 49\%$.

FIG. 4. Crystallization of GrGST films exhibiting different Ge excess: a) normalized integrated XRD intensity of the GST225(200) peak measured during in situ ramp annealing of 200 nm-thick films ($E_x = 0, 23, 42, 49$, and 61% , corresponding resp. to at% Ge of 22.5%, 40%, 55%, 60% and 70%), b) experimental T_x variations versus E_x determined from (a), c) total GST224 fraction variations versus time during KMC simulations of isothermal annealing of 50 nm-thick films (E_x

= 0, 20, 40, and 60%) at $T = 673$ K, and d) GST224 nucleation time variations versus E_x determined from (c).

FIG. 5. Normalized integrated XRD intensity variations of the peaks Ge(111) and GST225(200) measured during in situ ramp annealing of 200 nm-thick GrGST films: a) $E_x = 42\%$, b) $E_x = 49\%$, and c) $E_x = 61\%$.

FIG. 6. Normalized integrated XRD intensity variations of the peak GST225(200) measured during in situ isothermal annealing, and corresponding average size (L) of the GST225 grains deduced from the FWHM of the GST225(200) diffraction peak using the Scherrer equation: a) $E_x = 0$ and $T = 378$ K, and b) $E_x = 42\%$ and $T = 578$ K.

FIG. 7. Normalized integrated XRD intensity variations of the peak GST225(200) measured during in situ isothermal annealing of a 200 nm-thick GrGST film at $T = 578$ K with a) $E_x = 49\%$, and b) $E_x = 61\%$.

FIG. 8. KMC simulations of GrGST crystallization during isothermal annealing at 673 K: a) and b) simulation cell before and after GST224 crystallization for $E_x = 60\%$ in bulk and in a 50 nm-thick film, respectively; c) and d) phase fraction variations of the detected phases for $E_x = 20\%$ and $E_x = 40\%$, respectively, as well as corresponding simulation cells. Total GST224 corresponds to the sum of the phase fractions of GST224 and off-GST224.

FIG. 9. Normalized phase fraction variations of Ge and GST224 during KMC simulations of the crystallization of a 50 nm-thick GrGST film during isothermal annealing at 673 K: a) $E_x = 20\%$, b) $E_x = 40\%$, and c) $E_x = 60\%$.

FIG. 10. Temperature distribution along the GrGST film thickness (50 nm) used during KMC simulations of SET (blue solid line) and RESET operations. Two RESET conditions were used: RESET 1 (red solid line) and RESET 2 (orange dashed line). The black dashed line shows the melting temperature of GST224 (850 K).

FIG. 11. Microstructure evolution of a GrGST film with $E_x = 40\%$ during KMC simulation of five consecutive SET/RESET cycles using RESET 1: a) stoichiometric GST224 no seed, and b) non-stoichiometric GST224 with bottom seed.

FIG. 12. Microstructure of a GrGST film with $E_x = 40\%$ and stoichiometric GST224 after the fifth SET and RESET operations, using RESET 1 with a bottom seed layer (a) or with bottom and top seed layers (c), or using RESET 2 with a bottom seed layer (b) or with bottom and top seed layers (d); (e) schematics illustrating the evolution of the microstructure during cycling, from a GST-cluster structure to a GST-band structure.

FIG. 13. Microstructure of a GrGST film with $E_x = 40\%$ and non-stoichiometric GST224 after the fifth SET and RESET operations, using a) RESET 1, and b) RESET 2.

FIG. 14. Microstructure of a GrGST film with $E_x = 40\%$ and non-stoichiometric GST224 after the fifth SET and RESET operations, using RESET 1 with a bottom seed layer (a) or with bottom

and top seed layers (c), or using RESET 2 with a bottom seed layer (b) or with bottom and top seed layers (d).

Fig. 1

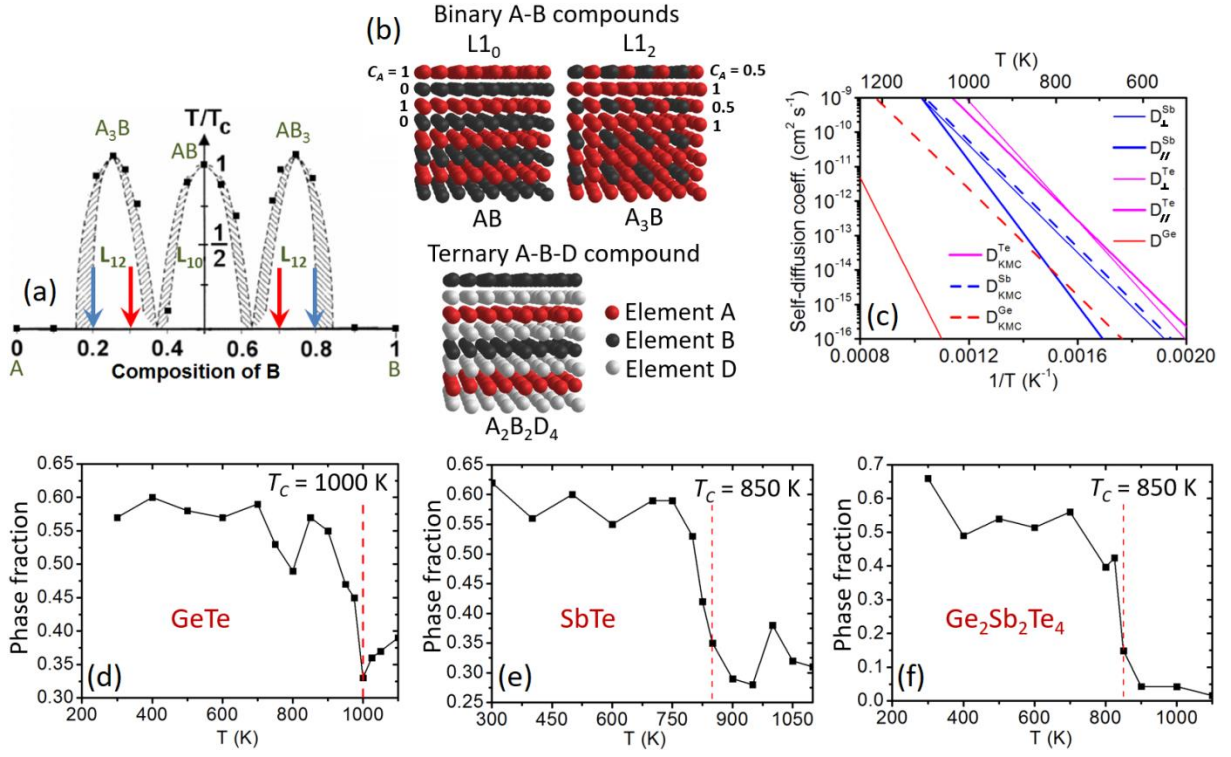


Fig. 2

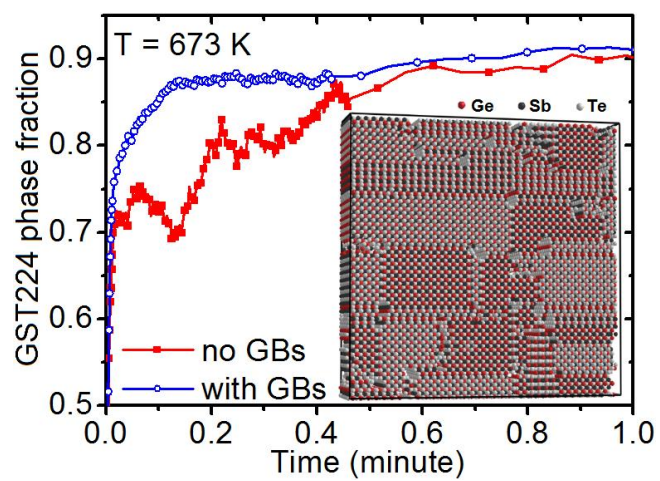


Fig. 3

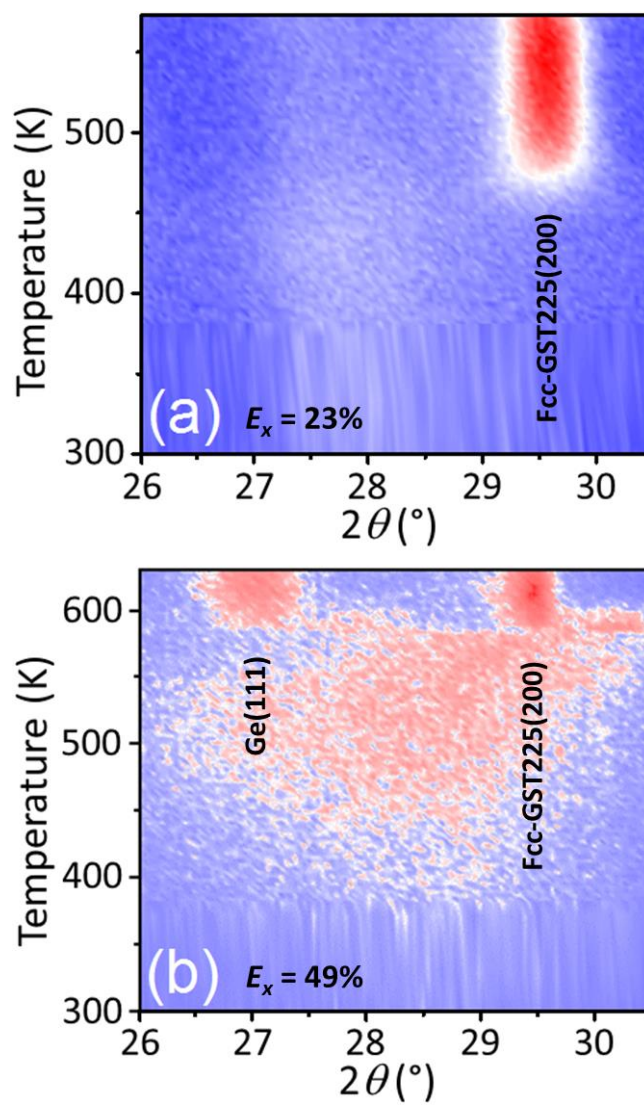


Fig. 4

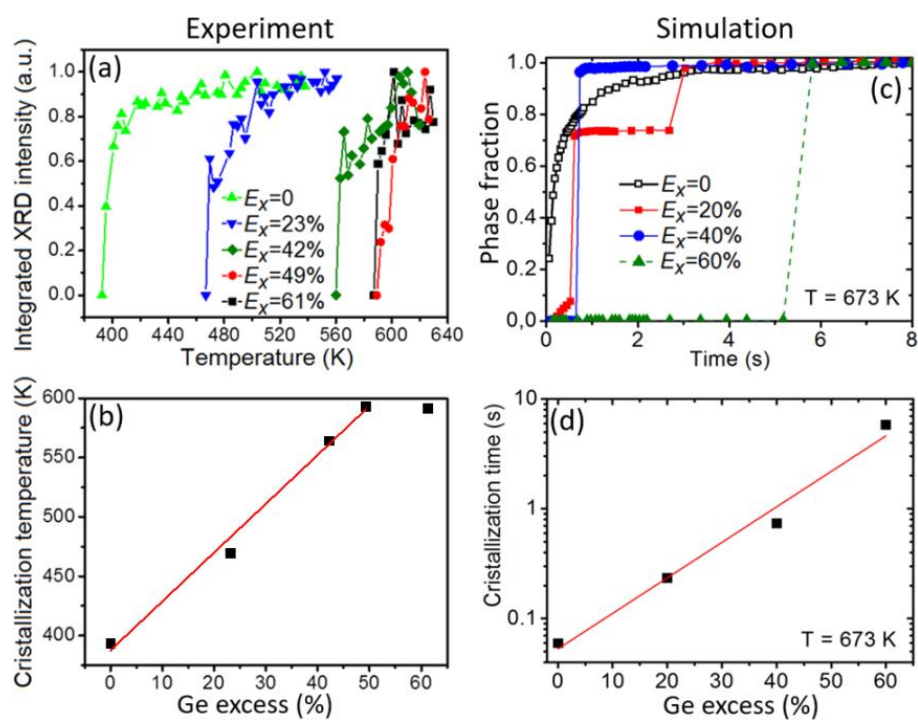


Fig. 5

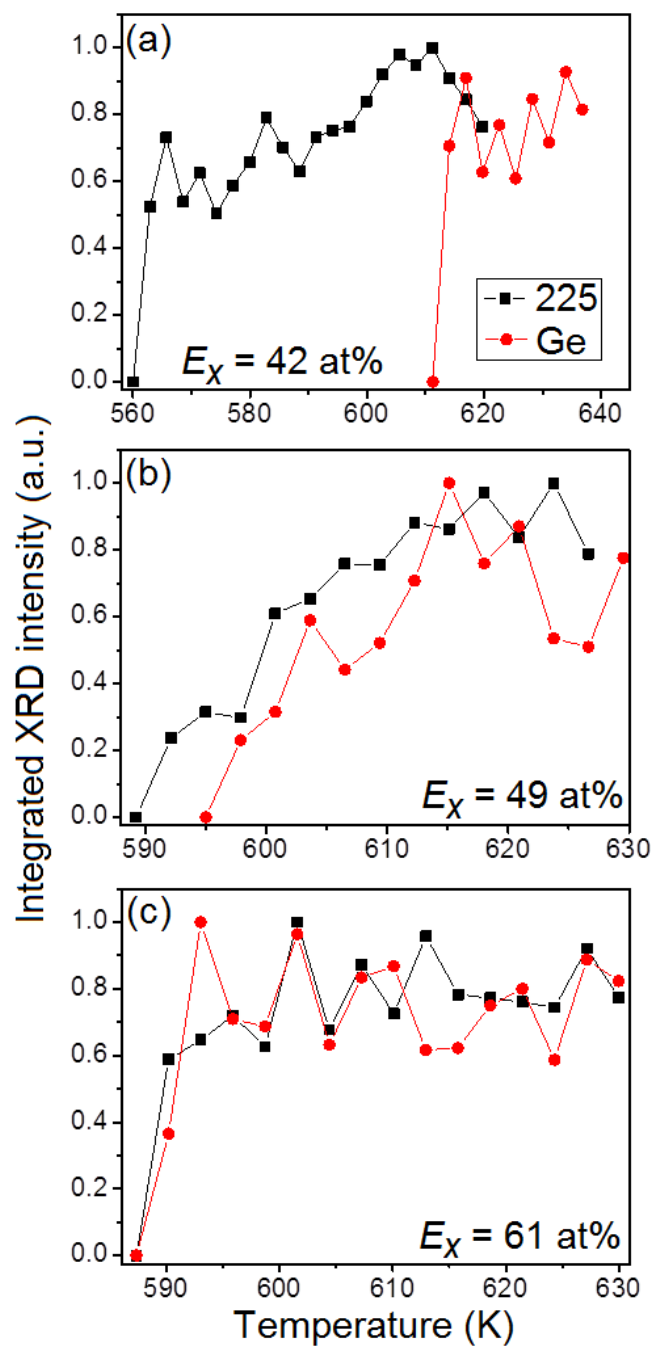


Fig. 6

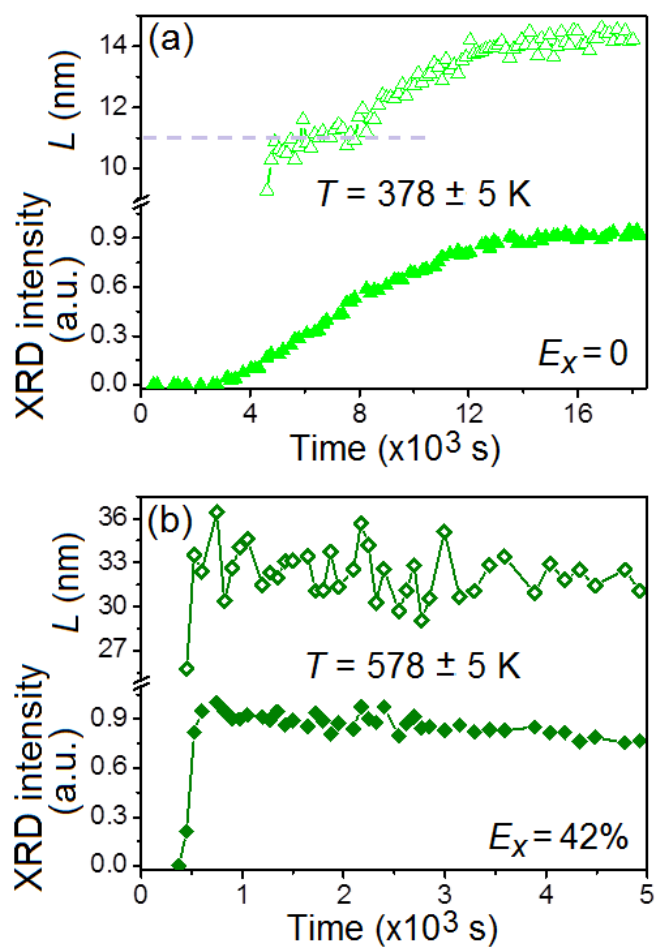


Fig. 7

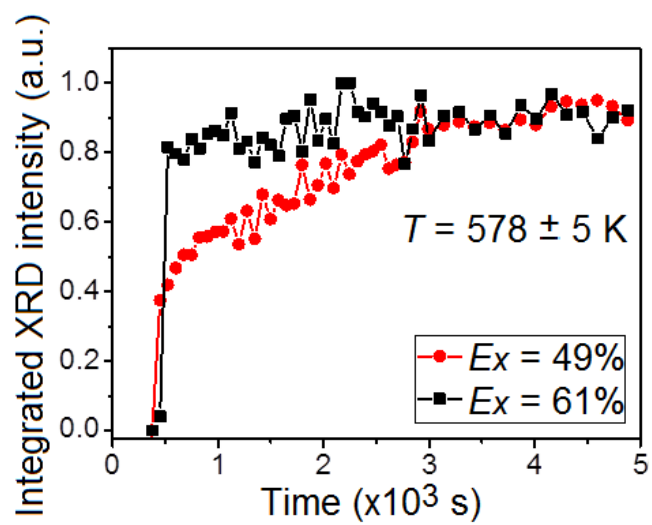


Fig. 8

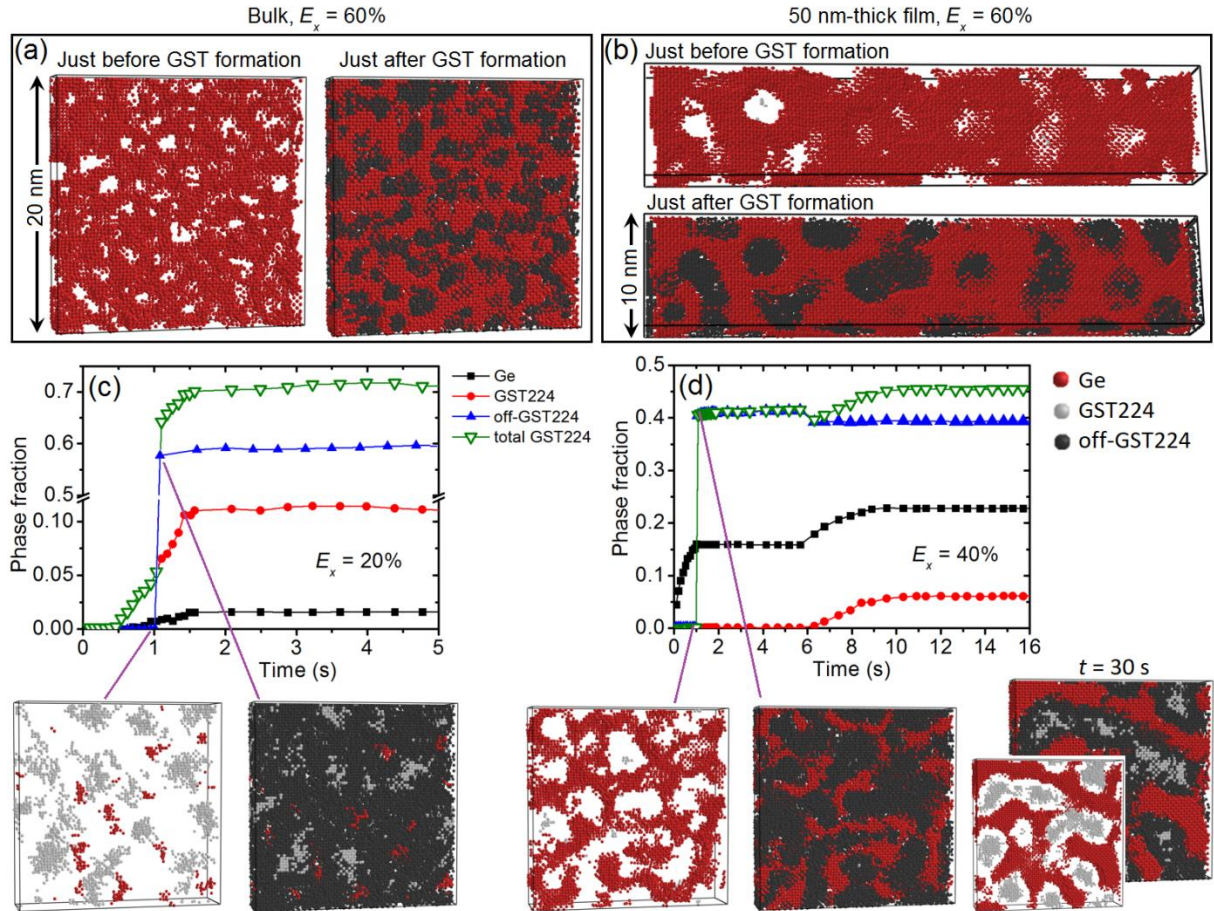


Fig. 9

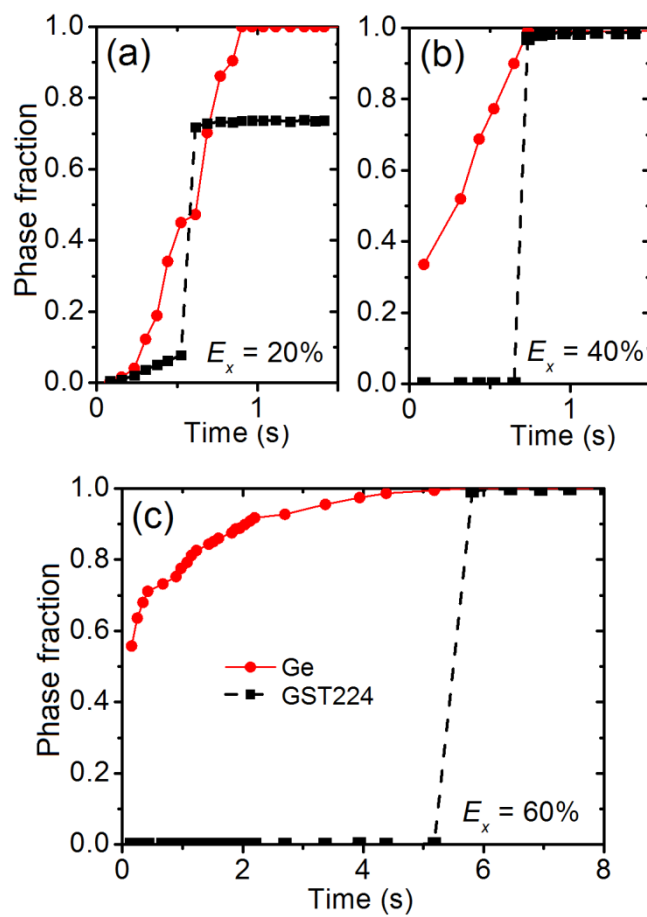


Fig. 10

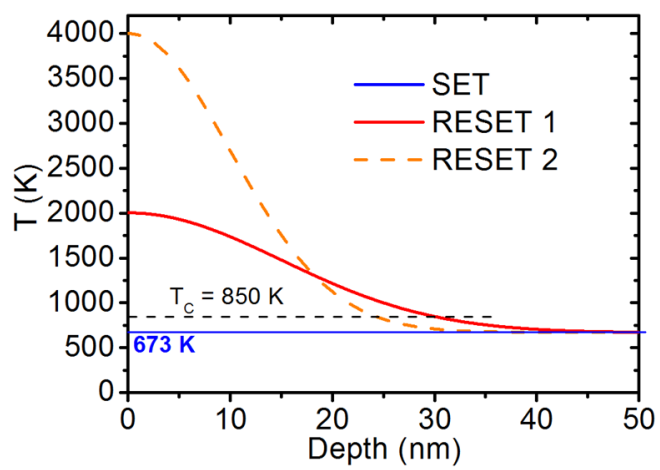
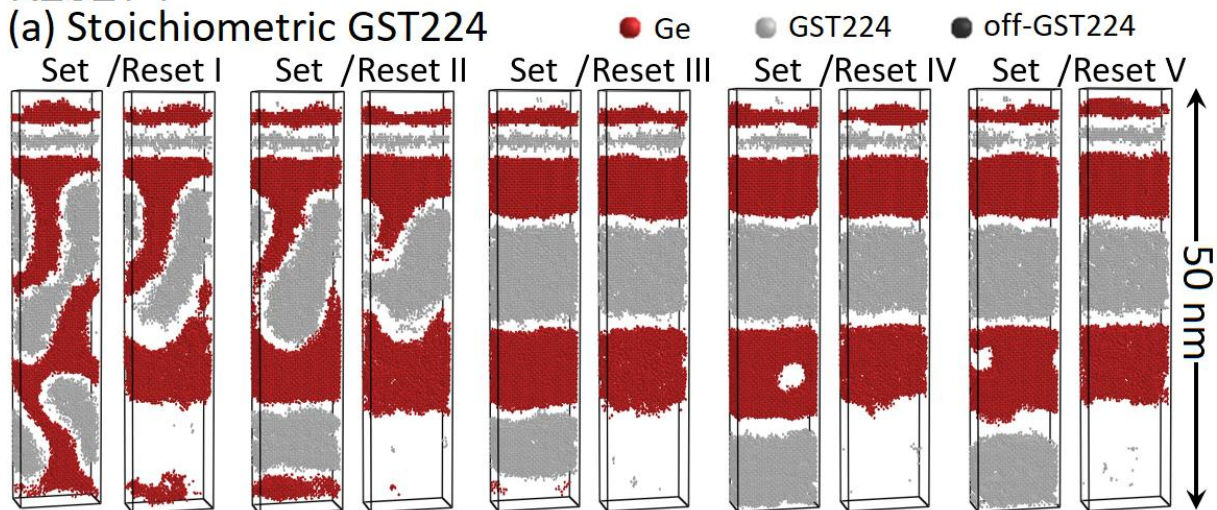


Fig. 11

RESET 1

(a) Stoichiometric GST224



(b) Off-stoichiometric GST224 with a bottom seed

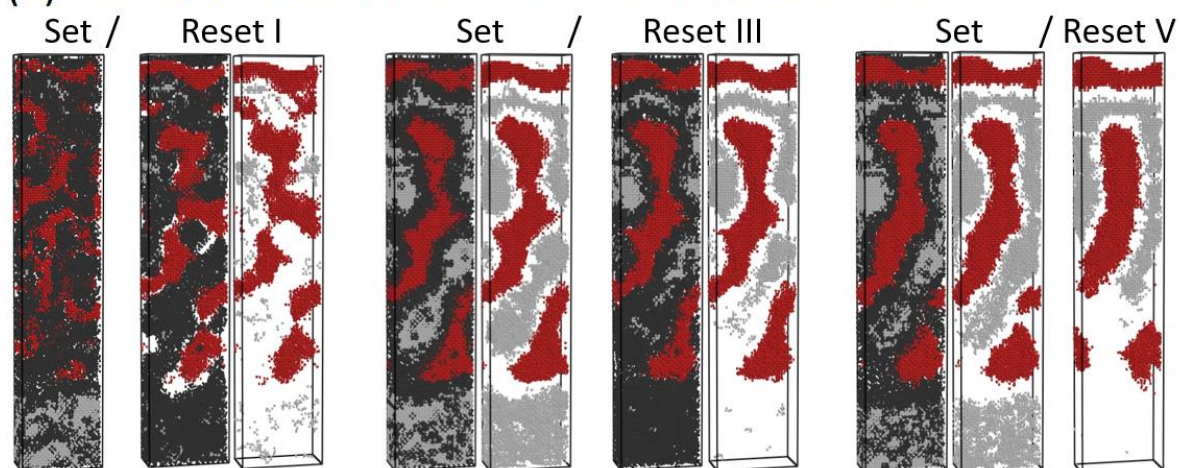


Fig. 12

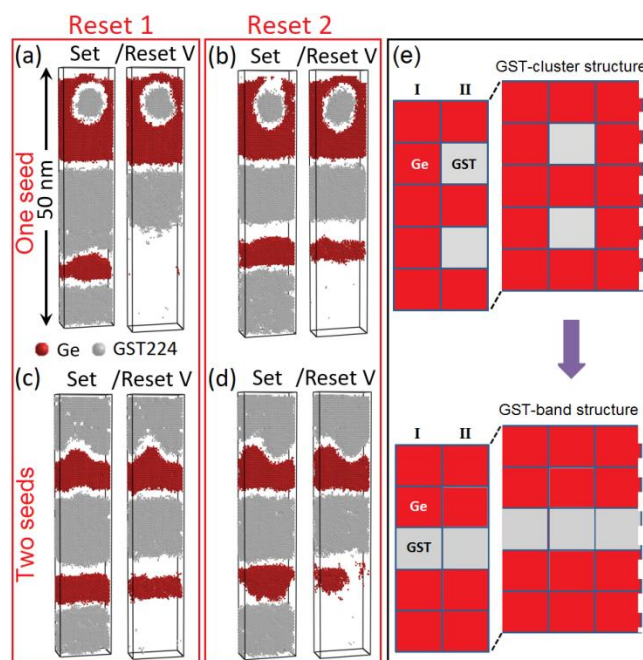


Fig. 13

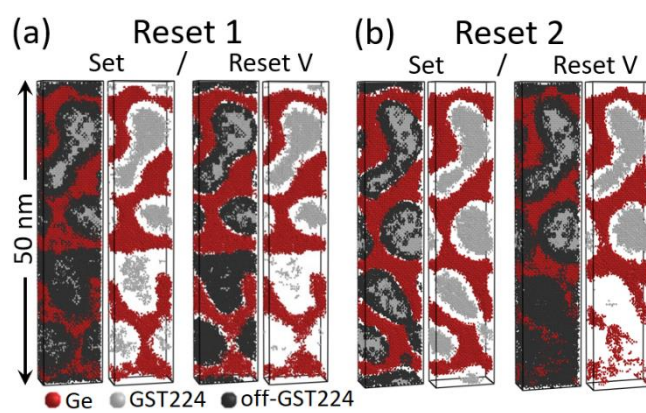


Fig. 14

